remote sensing

MDPI

Article

Estimating Global Gross Primary Production Using an Improved MODIS Leaf Area Index Dataset

Shujian Wang [1,2], Xunhe Zhang [1], Lili Hou [1,2], Jiejie Sun [2] and Ming Xu [1,2,3,*]

[1] College of Geography and Environmental Science, Henan University, Kaifeng 475004, China; wangsj@henu.edu.cn (S.W.); xunhezhang@henu.edu.cn (X.Z.); houlili@henu.edu.cn (L.H.)
[2] Guangdong-Hong Kong Joint Laboratory for Carbon Neutrality, Jiangmen Laboratory of Carbon Science and Technology, Jiangmen 529199, China; sunjj93@mail.ubc.ca
[3] BNU-HKUST Laboratory for Green Innovation, Advanced Institute of Natural Sciences, Beijing Normal University at Zhuhai, Zhuhai 519087, China
* Correspondence: mingxu@henu.edu.cn

Abstract: Remote sensing and process-coupled ecological models are widely used for the simulation of GPP, which plays a key role in estimating and monitoring terrestrial ecosystem productivity. However, most such models do not differentiate the C3 and C4 photosynthetic pathways and neglect the effect of nitrogen content on V_{max} and J_{max}, leading to considerable bias in the estimation of gross primary productivity (GPP). Here, we developed a model driven by the leaf area index, climate, and atmospheric CO_2 concentration to estimate global GPP with a spatial resolution of 0.1° and a temporal interval of 1 day from 2000 to 2022. We validated our model with ground-based GPP measurements at 128 flux tower sites, which yielded an accuracy of 72.3%. We found that the global GPP ranged from 116.4 PgC $year^{-1}$ to 133.94 PgC $year^{-1}$ from 2000 to 2022, with an average of 125.93 PgC $year^{-1}$. We also found that the global GPP showed an increasing trend of 0.548 PgC $year^{-1}$ during the study period. Further analyses using the structure equation model showed that atmospheric CO_2 concentration and air temperature were the main drivers of the global GPP changes, total associations of 0.853 and 0.75, respectively, while precipitation represented a minor but negative contribution to global GPP.

Keywords: ecological process model; photosynthesis; remote sensing data; carbon sink; SEM model; GPP; MODIS; LAI

check for updates

Citation: Wang, S.; Zhang, X.; Hou, Z.; Sun, J.; Xu, M. Estimating Global Gross Primary Production Using an Improved MODIS Leaf Area Index Dataset. *Remote Sens.* **2024**, *16*, 3731. https://doi.org/10.3390/rs16193731

Academic Editor: Huaqiang Du

Received: 3 August 2024
Revised: 27 September 2024
Accepted: 30 September 2024
Published: 8 October 2024

1. Introduction

Gross primary productivity (GPP) refers to the cumulative organic carbon sequestered by plants through photosynthesis within a specific region, corresponding to a combination of the amount of photosynthetically produced products and the total amount of organic carbon sequestered by green plants through photosynthesis per unit of area and time [1–4]. GPP is one of the most fundamental indicators of ecosystem productivity and plays a central role in studying global carbon cycling and climate change [5]. It not only determines the initial influx of matter and energy into terrestrial ecosystems but also serves as an important metric for the characterization of plant activities and ecological functions.

The most widely used models for estimation of global GPP are divided into ecological process models (the Biome-BGC model and BEPS model) [6–8] and light-use efficiency (LUE) models (GLO-PEM, MODIS, CASA, C-FIX, VPM, and BEAMS) [2,9–13], each of which has its advantages and disadvantages. The light-use efficiency model calculates GPP mainly based on photosynthetically active radiation, temperature, and light-use efficiency parameters related to vegetation type [14–16]. However, the light-use efficiency model does not fully capture the physiological processes of plants and is only suitable for large-scale GPP estimates. Ecological process-based models based on remote sensing data were improved by the Farquhar model, which draws upon the principles of biochemistry and

physics. These models have facilitated a deeper understanding and explanation of the biological mechanisms underlying photosynthesis. GPP product information can be found in Table 1.

The global distribution of C3 and C4 plants manifests distinct efficiencies in the assimilation of CO_2 during photosynthesis, altering the regional atmospheric CO_2 concentration and isotopic composition, thereby impacting the global carbon cycle [17]. Studies have revealed that C3 plants predominantly govern carbon absorption and GPP in temperate and high-latitude regions, whereas C4 plants assume significance in tropical and subtropical regions [18,19]. The distribution and influence of these two plant species might change considerably with climate change. C4 plants could expand their distribution and influence to more areas (including some traditional C3 plant areas), which could alter the carbon cycle and influence of these areas and, thus, affect the global carbon cycle and ecosystem productivity [17,20–22]. The nitrogen content in leaves influences the active amount and kinetic activity of RuBisCO, as well as the temperature-standardized rate of maximum RuBisCO carboxylation (V_{cmax25}), thereby affecting the rate of plant photosynthesis [23].The terrestrial carbon cycle model is highly sensitive to the maximum carboxylation rate (V_{cmax}) and the maximum electron transport rate (J_{max}) derived from V_{cmax25} during photosynthesis, which are influenced by leaf nitrogen content and plant nitrogen uptake [24]. However, current ecological models only couple the C3/C4 plant processes in the Community Land Model (CLM) and do not generate data products. Consequently, it is necessary to develop a model that can quickly and stably estimate global GPP on a large scale while coupling the C3/C4 processes and leaf nitrogen content with photosynthesis so as to reduce significant errors in the estimation of global GPP caused by current models.

The model we developed is driven by the leaf area index (LAI), distinguishes between C3 and C4 plants, optimizes the effects of nitrogen content on V_{cmax} and J_{max}, and captures the physical and chemical information of the surface, improving the accuracy of GPP simulation. This study aims to (1) develop a moderate-resolution GPP dataset with a spatial resolution of 0.1 degree and a temporal resolution of one day, (2) use the above model to estimate the global GPP from 2000 to 2022, and (3) identify the key drivers of global annual GPP.

Table 1. GPP product information. EPM: ecological process model; LUE: light-use efficiency; ML: machine learning; VOD: vegetation optical depth; SIF: solar-induced fluorescence; Region: country/continent; Pathway: photosynthetic pathway.

Dataset	Method	Pathway	Temporal Resolution	Spatial Resolution	Unit	Study Period	Spatial Coverage	Reference
BEPS	EPM	C3	day	0.07°	gC/m^2	1981–2019	Global	Jv et al. (2021) [25]
BESS	EPM	C3	day	0.05°	gC/m^2	1982–2019	Global	Li et al. (2023) [26]
EC-LUE	LUE	C3/C4	8 days	0.05°	kgC/m^2	1982–2018	Global	Zhang et al. (2020) [4]
MODIS	LUE	C3/C4	8 days	500 m	kgC/m^2	2003–2022	Global	Running et al. (2021) [27]
VPM	LUE	C3/C4	8 days	0.05°	kgC/m^2	2000–2016	Global	Zhang et al. (2017) [3]
Random Forest	ML	C3	10 days	0.10°	gC/m^2	1999–2020	Global	Zeng et al. (2020) [28]
VODCA2GPP	VOD	C3	8 days	0.25°	gC/m^2	1988–2020	Global	Benjamin et al. (2022) [29]
GLO–PEM	LUE	C3/C4	8 days	10 m	gC/m^2	1981–2023	China	Stephen et al. (1995) [10]
GLASS	LUE	C3	8 days	0.05°	gC/m^2	1981–2018	Global	Liang et al. (2021) [30]
FluxSat v2.0	ML	C3	day	0.05°	gC/m^2	2000–2020	Global	Joiner et al. (2019) [31]
SMUrF	SIF	C3	4 days	0.05°	gC/m^2	2010–2019	Region	Wu et al. (2021) [32]
SiB4	EPM	C3/C4	Monthly	0.50°	gC/m^2	2000–2018	Global	Haynes et al. (2021) [33]
SMAP L4	EPM	C3	day	0.09°	gC/m^2	2015–2024	Global	Kimball et al. (2021) [34]
CARDAMOM	EPM	C3	day	0.50°	gC/m^2	2001–2016	USA	Yang et al. (2021) [35]
NIRv-Index	SIF	C3	day	0.05°	gC/m^2	1982–2018	Global	Wang et al. (2020) [36]
PML-V2	LUE	C3/C4	Monthly	0.05°	gC/m^2	1982–2014	Global	Zhang et al. (2020) [37]
PML-V2	LUE	C3/C4	8 days	0.05°	gC/m^2	2002–2019	Global	Chen et al. (2019) [38]
BCC-ESM1	EPM	C3/C4	Monthly	2.81°	gC/m^2	1850–2014	Global	Wu et al. (2020) [39]
CNRM-CM6-1	EPM	C3/C4	Monthly	1.41°	gC/m^2	1850–2014	Global	Program et al. (2019) [40]
Neural Network	ML	C3	4 days	0.05°	gC/m^2	2000–2022	Global	Zhang et al. (2018) [41]
MuSyQ	LUE	C3	8 days	0.05°	gC/m^2	1981–2018	Global	Wang et al. (2021) [42]
Blue Carbon	EPM	C3	16 days	250 m	gC/m^2	2000–2019	USA	Fergin et al. (2020) [43]

2. Methods and Data

2.1. Model Description

The direct and diffuse components of the total incident radiation were partitioned, with this partitioning process being determined by the proportion of cloud cover [44–46]. We applied two-stream radiative transfer approximation, which accounted for multiple scatterings within a finite canopy [44,46]. We implemented different scattering coefficients for direct and diffuse radiation, ensuring that the unique characteristics of the two radiation types were accurately represented [46]. The methods mentioned above allowed us to quantify the transmission and reflection factors for both direct and diffuse radiation, providing a detailed understanding of the interactions between canopy and radiation [46,47]. We integrated the two-leaf model with canopy radiation transfer to quantify the radiation absorption for both sunlit and shaded leaves [48,49]. The Ball–Berry–Leuning (BBL) stomatal conductance model was integrated into the photosynthesis process, optimizing the balance between CO_2 uptake and water conservation [50]. Moreover, the calculation of the exact duration of global photosynthesis through sunrise, sunset, and local time computations facilitated a more accurate estimation of GPP. Finally, given the hourly time resolution of the data, accurately calculating the specific times for photosynthesis during sunrise and sunset in the respective time zone required precise determination of the daylight proportion in that zone (Appendix A).

We improved the corresponding variables of the Farquhar model for C3 plants [51] and the Collatz model for C4 [52] by integrating V_{max}, J_{max}, and Rd from the CLM model in the photosynthesis module [24,53]. The parameters of V_{cmax25}, J_{max25}, and Rd_{25} were scaled over the canopy for sunlit and shaded leaves and were adjusted for leaf temperature. The maximum rate of carboxylation at 25 °C (V_{cmax25}) varied with foliage nitrogen concentration, the fraction of leaf nitrogen in Rubisco, and the weight proportion of Rubisco relative to its nitrogen content [23]. A flow chart of the implementation of the proposed model by parallel computation with GPU is presented in Figure 1.

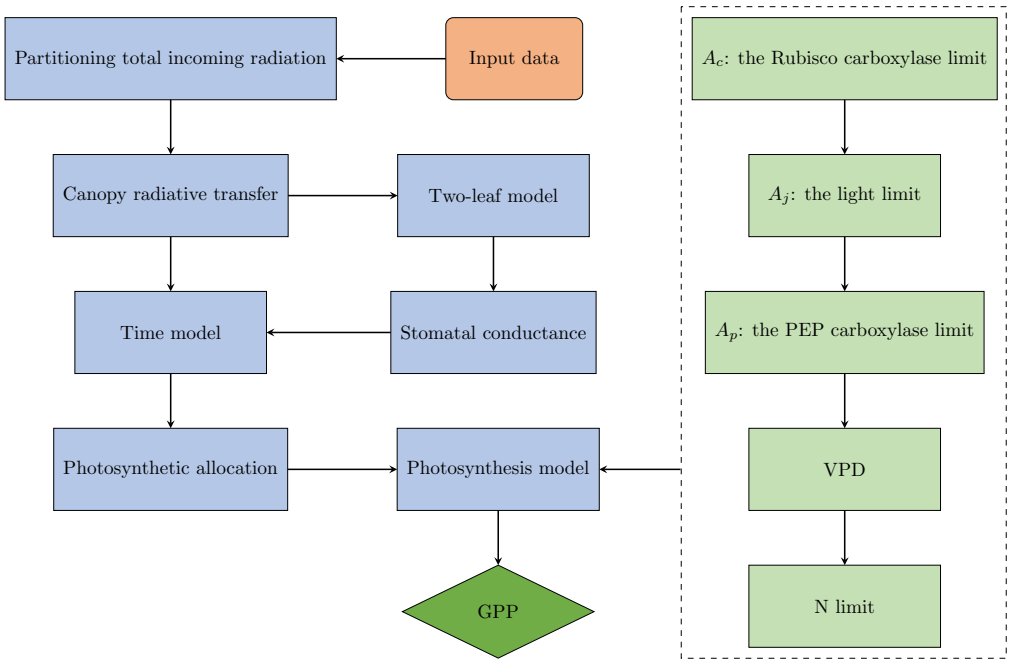

Figure 1. Flow chart of the proposed model.

The proposed model incorporates seven input variables, but the forcing variables had to be resampled to align with the spatio-temporal resolution of the climate variables, as the spatio-temporal resolution for their metadata did not match (Table 2).

Table 2. The input datasets of the proposed model. GPP: gross primary productivity simulated by the proposed model; C3/C4: the percentage of C4 plants in pixels; CI: clumping index; D2m: 2m dewpoint temperature; T2m: 2 m air temperature; SSRD: surface solar radiation downwards; LAI: leaf area index; Landcover: vegetation types.

Product	Spatial Resolution	Temporal Resolution	Study Period	Reference
GPP	0.1° × 0.1°	1-Day	2000–2022	(This study)
C3/C4	0.1° × 0.1°	1-Year	Mean	Still et al., 2003 [18]
CI	0.1° × 0.1°	1-Year	2001–2019	Fang & Wei, 2021 [54]
D2m	0.1° × 0.1°	1-Hour	2000–2022	Balsamo et al., 2015 [55]
T2m	0.1° × 0.1°	1-Hour	2000–2022	Balsamo et al., 2015 [55]
SSRD	0.1° × 0.1°	1-Hour	2000–2022	Muñoz Sabater, 2019 [56]
LAI	0.1° × 0.1°	1-Day	2000–2022	Barnes et al., 2003 [57]
Landcover	0.1° × 0.1°	1-Year	2000–2022	Barnes et al., 2003 [57]

2.2. Data Source

2.2.1. Data from Flux Tower

The FLUXNET2015 dataset is a comprehensive and valuable collection of eddy covariance measurements obtained from various ecosystems around the world. FLUXNET2015 represents a collaborative effort involving multiple research institutions and networks. It encompasses measurements from a wide range of ecosystems, including forests, grasslands, croplands, wetlands, and more. The FLUXNET community comprises datasets on energy fluxes, carbon fluxes, and meteorological variables collected and processed at various sites—crucial for studying global ecosystem function and response [3]. More information is available at the FLUXNET website (https://fluxnet.org/data/fluxnet2015-dataset/ (accessed on 28 September 2024)).

The GPP (GPP_NT_VUT_REF) of the FLUXNET2015 dataset's eddy covariance flux towers was used in comparison with our model's GPP in this study. We estimated the global GPP values using our model and extracted the model-estimated GPP value of each corresponding point of the flux tower sites by latitude and longitude [4]. Then, we selected 128 flux tower sites around the world (Figure 2) to validate the results of our model by removing outliers. Information about the flux tower sites used in this study is shown in Appendix B.

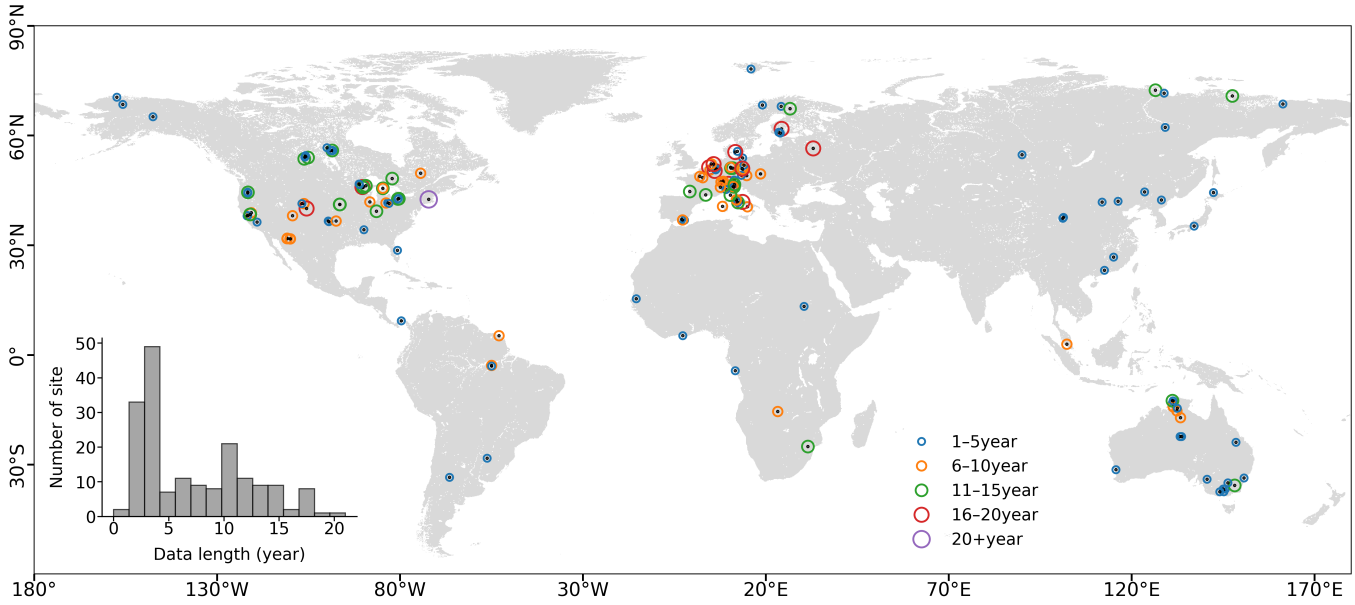

Figure 2. Map of 128 tower sites included in this paper from the FLUXNET2015 dataset. The size of the circle indicates the length of the data record. The inset shows the distribution of data record lengths.

2.2.2. Data Driving the Model

ERA-Interim is a widely used reanalysis dataset that provides comprehensive and high-quality global atmospheric and surface parameters spanning several decades [55,58]. ERA-Interim, developed by the European Centre for Medium-Range Weather Forecasts (ECMWF), offers a wealth of information on atmospheric variables such as wind, temperature, humidity, and pressure, as well as surface parameters like sea ice, sea surface temperature, and soil moisture. The dataset contains 69 global variables with a temporal and spatial resolution of 1 h and 0.1 degree, respectively. We applied two variables from the reanalysis dataset as driving variables for the model, including 2 m temperature (T2m; K) and 2 m dewpoint temperature (D2m; K).

Google Earth Engine (GEE), developed by Google, is a cloud-based geospatial computing platform designed to allow users to leverage Google's powerful computing power and computing resources to analyze and process large amounts of geospatial data [59,60]. It integrates satellite imagery, geospatial datasets, and other Earth observation data to support a wide range of applications in environmental monitoring, land use analysis, disaster response, and more. The global surface solar radiation downwards (SSRD) at a 0.1-degree spatial resolution and 1-h temporal resolution was extracted from the dataset [56].

MODIS, which stands for Moderate-Resolution Imaging Spectroradiometer, is a state-of-the-art Earth observation instrument aboard the NASA Terra and Aqua satellites [57,61]. Its broad spectral coverage allows it to monitor a variety of Earth processes, including cloud cover, sea surface temperature, vegetation status, land cover changes, and more. We retrieved two variables from the dataset, namely leaf area index (LAI, m^2m^{-2}), with a temporal and spatial resolution of 4 days and 500 m, respectively, and vegetation types (Landcover), with a temporal and spatial resolution of one year and 500 m, respectively. We obtained LAI data with a temporal resolution of 1 day by removing outliers [62] and fitting the double logistic equation [63] and data with a spatial resolution of 0.1 degree by resampling.

The accurate simulation of water, carbon, and energy exchanges between the atmosphere and biosphere relies heavily on understanding the global distribution of C3 and C4 plants. The distinctive physiological and functional characteristics of these plant types play a pivotal role. To achieve this understanding, we utilized the 1-degree spatial distribution map of global C3 and C4 vegetation [17]. This incorporation of the distribution data enabled us to account for the diverse physiological processes inherent to C3 and C4 vegetation, thereby enhancing the precision of our simulations.

The vegetation clumping index (CI) quantifies the degree of deviation from the random distribution of leaves and serves as an important structural parameter of the canopy that controls photosynthesis and evapotranspiration processes in terrestrial ecosystems [64,65]. The global clumping index (CI), with a temporal and spatial resolution of 8 days and 500 m, respectively, was download from National Ecological Science Data Center [54].

2.3. Computation Platform

The proposed model was run a desktop PC with an Ubuntu 22.04 system equipped with 12 Intel i7-12700K cores running at 3.6 GHz with 128 GB of memory. The NAS delivers network storage solutions that excel in performance, fault tolerance, and data security, powered by an AMD Ryzen V1500B 2.2 GHz processor and 16 GB of memory. It offers a storage capacity of 128 TB, utilizing eight 16 TB hard disks (WUH721816ALE6L4-16TB) configured in a RAID10 array. Our model leverages OpenMP acceleration technology, enabling high-precision, large-scale parallel computations of various driving factors for GPP modeling.

2.4. Data Analysis

We analyzed the relevance of different models for the estimation of GPP and the sensitivity of GPP to environmental variables. The analyses were performed using the R version 4.3.3 programming language, along with the appropriate packages [66]. Pearson

correlation analysis and the Shapiro–Wilk normality test were carried out using functions from the stats package [66], specifically utilizing the "cor.test" and "shapiro.test" functions. The structural equation model was built by employing the "psem" function, which is available in the piecewiseSEM package [67].

Structural Equation Modeling (SEM) is a statistical method that is used to analyze the relationships between several variables [67,68]. SEM combines elements of factor analysis and path analysis and enables the simultaneous investigation of relationships between observed variables and latent variables [67–69]. This approach allows for the modeling of complex multivariable relationships [70].

3. Results

3.1. Model Validation

We compared the mean annual GPP estimated from flux towers with the mean annual GPP simulated by the proposed model (Figure 3). We found that the proposed model accounted for 72.3% of the spatial variability in GPP across all validation sites. The proposed model performed very well at most sites, with a statistically significant p value < 0.01. The mean relative RMSE (RRMSE) and mean bias over all the sites were 36.3% and 9.23% gC m^{-2} $year^{-1}$, respectively. The relative root mean square error (RMSE) values comparing the observed data and the simulated data for each site are shown in Appendix B.

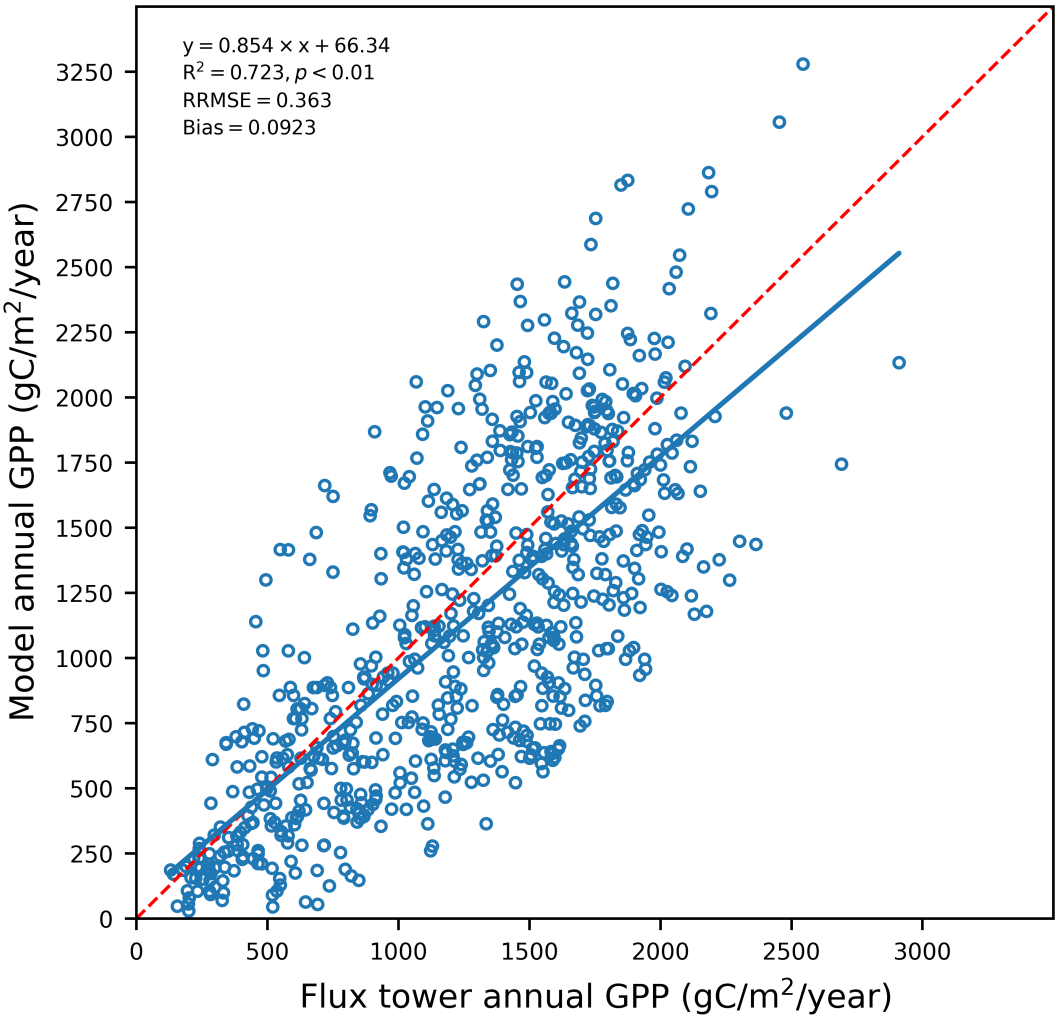

Figure 3. Comparison of annual GPP estimated from flux towers and annual GPP simulated by the proposed model. The blue line is the regression line, and the red dashed line is the 1:1 line. The regression equation, correlation coefficients, statistical significance, relative mean square error, and bias are shown on the top.

3.2. The Dynamic of Global GPP from 2000 to 2022

The long-term trend of annual global summed GPP simulated by the proposed model, BEPS [71–73], MODIS [27], and VPM [3] shows an increase over the time series (Figure 4). The proposed model quantified the annual global GPP between 116.4 PgC year^{-1} and 133.94 PgC year^{-1}, averaging 125.93 PgC year^{-1} from 2000 to 2022. In contrast, the BEPS model produced annual global summed GPP estimates ranging from 117.04 PgC year^{-1} to 129.92 PgC year^{-1}, averaging 122.98 PgC year^{-1} from 2000 to 2019. Additionally, the MODIS model simulated annual global summed GPP ranging from 95.28 PgC year^{-1} to 103.92 PgC year^{-1}, averaging 99.1 PgC year^{-1} from 2003 to 2022. Lastly, another VPM model simulation of annual global summed GPP spanned 116.67 PgC year^{-1} to 126.29 PgC year^{-1}, averaging 121.09 PgC year^{-1} from 2000 to 2017. We found a significant increasing trend for the proposed model, BEPS, MODIS, and VPM, with average increase rates of 0.548 PgC year^{-1}, 0.685 PgC year^{-1}, 0.34 PgC year^{-1}, and 0.53 PgC year^{-1} globally, respectively. A significance test of the increasing trend showed that all p values were below 0.01. The GPP values estimated by the proposed model showed correlations of 0.767, 0.765, and 0.657 with those of the BEPS, VPM, and MODIS models, respectively. All significance test p values were below 0.01 (Table 3).

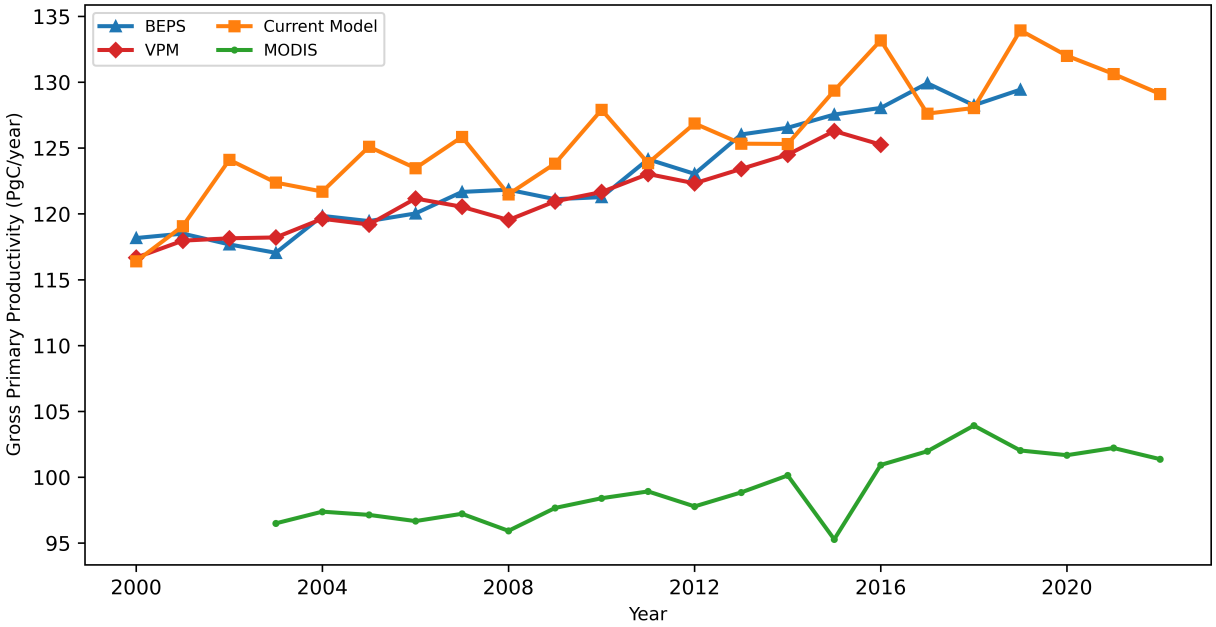

Figure 4. Comparisons of annual global summed GPP estimates from various models.

Table 3. Statistical analysis of GPP for the proposed model, BEPS, VPM, and MODIS.

Model	R^2 (Compared to Our Study)	p Value (Compared to Our Study)	Linear Regressions	R^2	p Value
Our study	1	<0.001	$y = 0.548x - 976.06$	0.8633	<0.001
BEPS	0.767	<0.001	$y = 0.685x - 1253.23$	0.9758	<0.001
MODIS	0.657	<0.001	$y = 0.34x - 585.61$	0.8077	<0.001
VPM	0.765	<0.001	$y = 0.536x - 935.68$	0.9636	<0.001

3.3. The Spatial Pattern of Global GPP

The spatial patterns of the mean annual GPP simulated by the proposed model, BEPS, MODIS, and VPM are generally consistent (Figure 5). The proposed model estimated the mean annual GPP to range from 0 KgC m^{-2} year^{-1} to 4.0 KgC m^{-2} year^{-1}, with an average of 0.837 KgC m^{-2} year^{-1} during the study period of 2000 to 2022 (Figure 5A). In contrast, the BEPS model produced an annual GPP of 0.002 KgC m^{-2} year^{-1} to 3.89 KgC m^{-2} year^{-1}, with an average of 1.02 KgC m^{-2} year^{-1} from 2000 to 2019 (Figure 5B). Additionally,

the MODIS model simulated the mean annual GPP to span from 0 KgC m^{-2} $year^{-1}$ to 3.5 KgC m^{-2} $year^{-1}$, with an average of 0.711 KgC m^{-2} $year^{-1}$ from 2003 to 2022 (Figure 5C). Lastly, the VPM model simulated the mean annual GPP to range from 0 KgC m^{-2} $year^{-1}$ to 4.29 KgC m^{-2} $year^{-1}$, with an average of 0.88 KgC m^{-2} $year^{-1}$ from 2000 to 2017 (Figure 5D). We observed that the peak annual GPP values occurred predominantly in tropical regions, particularly within the evergreen broadleaf forests of the Amazon and Southeast Asia, while the lowest GPP values were primarily situated in cold and arid areas.

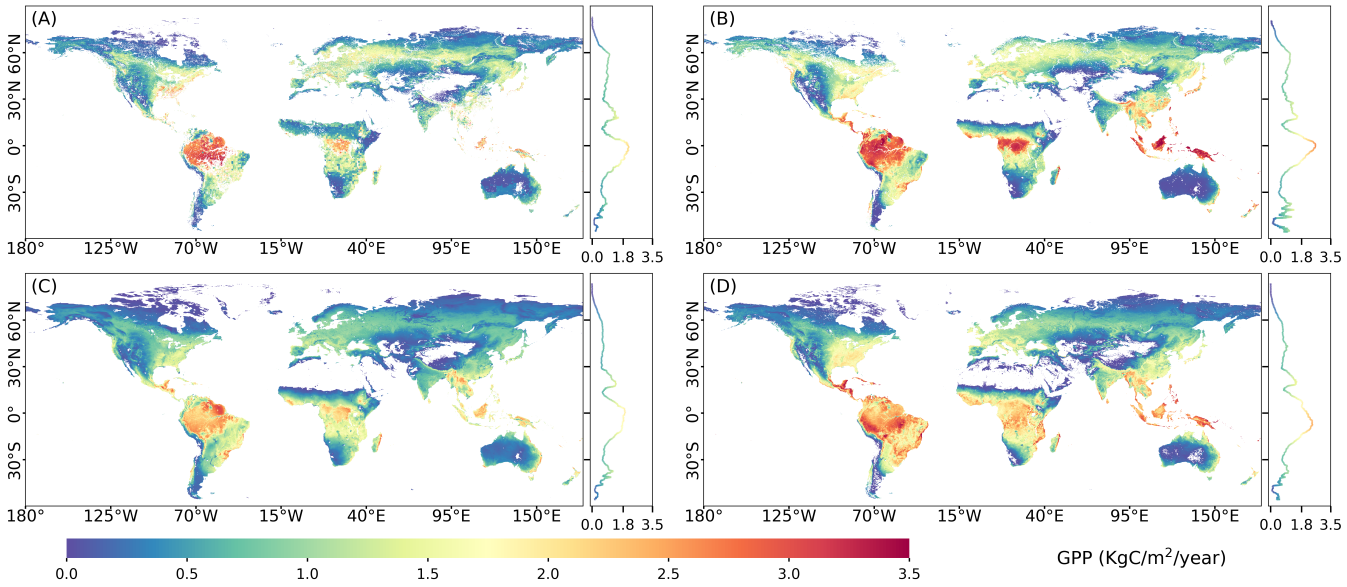

Figure 5. Comparisons of annual global summed GPP estimates from various models and the average value of latitude variation. (**A**) Proposed model; (**B**) BEPS; (**C**) MODIS; (**D**) VPM.

The long-term trend of GPP was analyzed by the linear regression method (Figure 6). The global GPP showed an increasing trend of 72.7%, 85.7%, 68.1%, and 78.3% for the proposed model, BEPS, MODIS, and VPM, respectively (Figure 6). The statistically significant trends at a 95% confidence level were 46.03%, 62.03%, 30%, and 56.7% for the current model, BEPS, MODIS, and VPM, respectively. These significant increases were predominantly found in regions across Europe, Southeast Asia, and Africa. The significantly decreasing trends of global terrestrial production were 17.23%, 15.1%, 6.5%, and 21.7% for the proposed model, BEPS, MODIS, and VPM, respectively. These trends were distributed across various locations and particularly notable in tropical rainforests such as the Congo Basin and the Amazon. These spatial patterns in annual mean GPP trends, along with the updated estimates extending to 2022, are consistent with findings from previous studies [74].

The apparent discrepancy between the positive GPP trend from 2000 to 2022 (Figure 4) and the negative values in the global spatial distribution of GPP (Figure 6) could be clarified by distinguishing between temporal trends and spatial patterns. Figure 4 shows the overall global GPP trend, indicating an increase in average GPP over time. In contrast, Figure 6 shows the spatial distribution of GPP at 0.1-degree resolution, with individual pixels reflecting localized changes in structural, climatic, and physiological parameters of C3 and C4 vegetation. While the global average GPP trend is positive, localized declines occurred in certain regions due to factors such as climate change or land use change. Even though the global GPP trend is upward, the higher-resolution spatial data showed more local fluctuations, which do not contradict the overall positive trend.

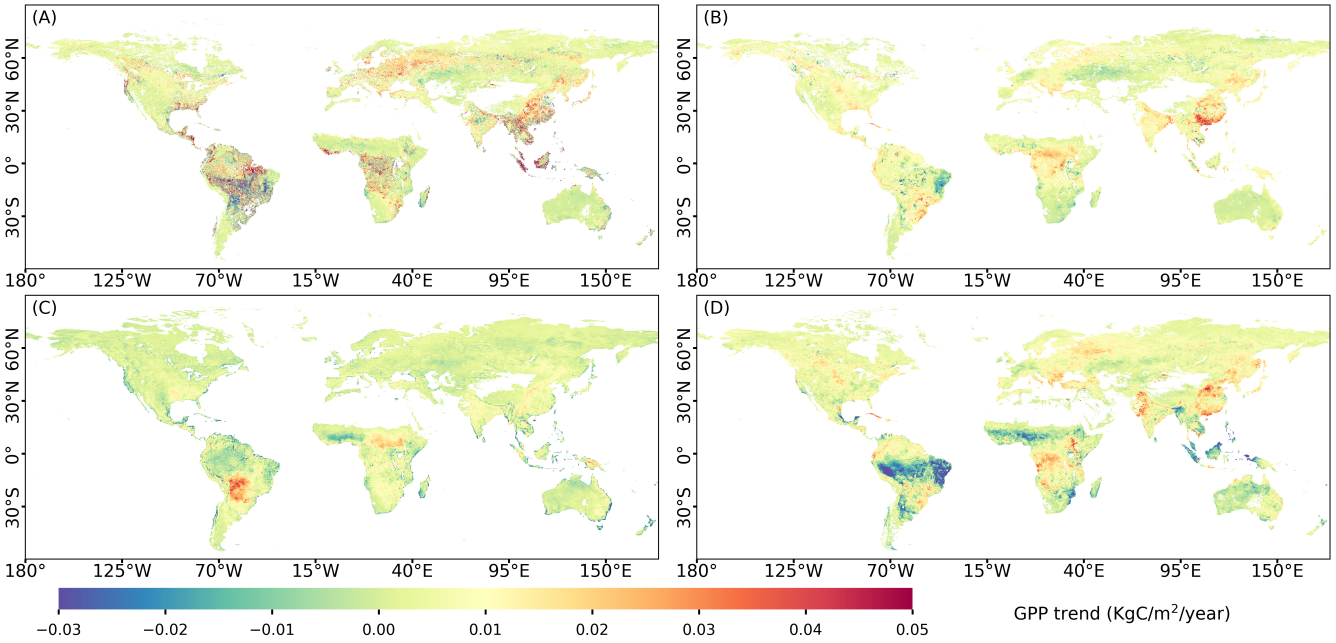

Figure 6. Spatial pattern of global GPP (KgC m^{-2} $year^{-1}$) trend simulated by (**A**) the proposed model, (**B**) BEPS, (**C**) MODIS, and (**D**) VPM.

4. Discussion

4.1. Environmental Characteristics of Flux Towers Suitable for Validating GPP

The flux sites we selected for comparison are characterized by relatively homogeneous land surface types, with minimal heterogeneity or topographical differences in the surrounding areas [75]. This uniformity helped to minimize potential errors caused by surface complexity when comparing lower-resolution global data with higher-resolution flux tower data [76]. In addition, the uniformity of terrain, vegetation types, and climatic conditions around the flux sites improved the feasibility and reliability of the comparison [77]. This analysis allowed us to more effectively assess the applicability and accuracy of global datasets in specific regions, providing a solid foundation for data model refinement and optimization [78].

In this study, we compared the environmental variables of the flux sites with those of the surrounding areas within a radius of 5 km, focusing on the distribution of elevation, leaf area index (LAI), and vegetation types. We compared the elevation of the flux sites with the average elevation in the surrounding 5 km and found that a correlation coefficient of 98.5% and statistical significance of $p < 0.01$ indicate a high degree of consistency (Figure 7A). We also compared the average annual LAI of the site with the average annual LAI of the area within 5 km, which resulted in a correlation coefficient of 98.5% and statistical significance of $p < 0.01$, also indicating a strong similarity (Figure 7B). We calculated the ratio of vegetation types at the site to vegetation types within a 5 km radius of the site (Figure 7C). The results showed that the average proportions for CRO, DBF, DNF, EBF, ENF, GRA, MF, OSH, SAV, WET, and WSA were 0.92, 0.81, 0.80, 0.90, 0.78, 0.92, 0.89, 0.90, 0.97, 0.90, and 0.86, respectively. This indicates that the flux site data adequately represent their spatial environment [79,80]. These results confirm the reliability of the flux site data and provide important evidence for its application in large-scale environmental studies [81]. These consistent environmental characteristics indicate that the climatic and ecological conditions in the region are relatively stable, which helps to minimize the fluctuations in meteorological data caused by terrain variations and ensure more reliable data collection at the flux towers.

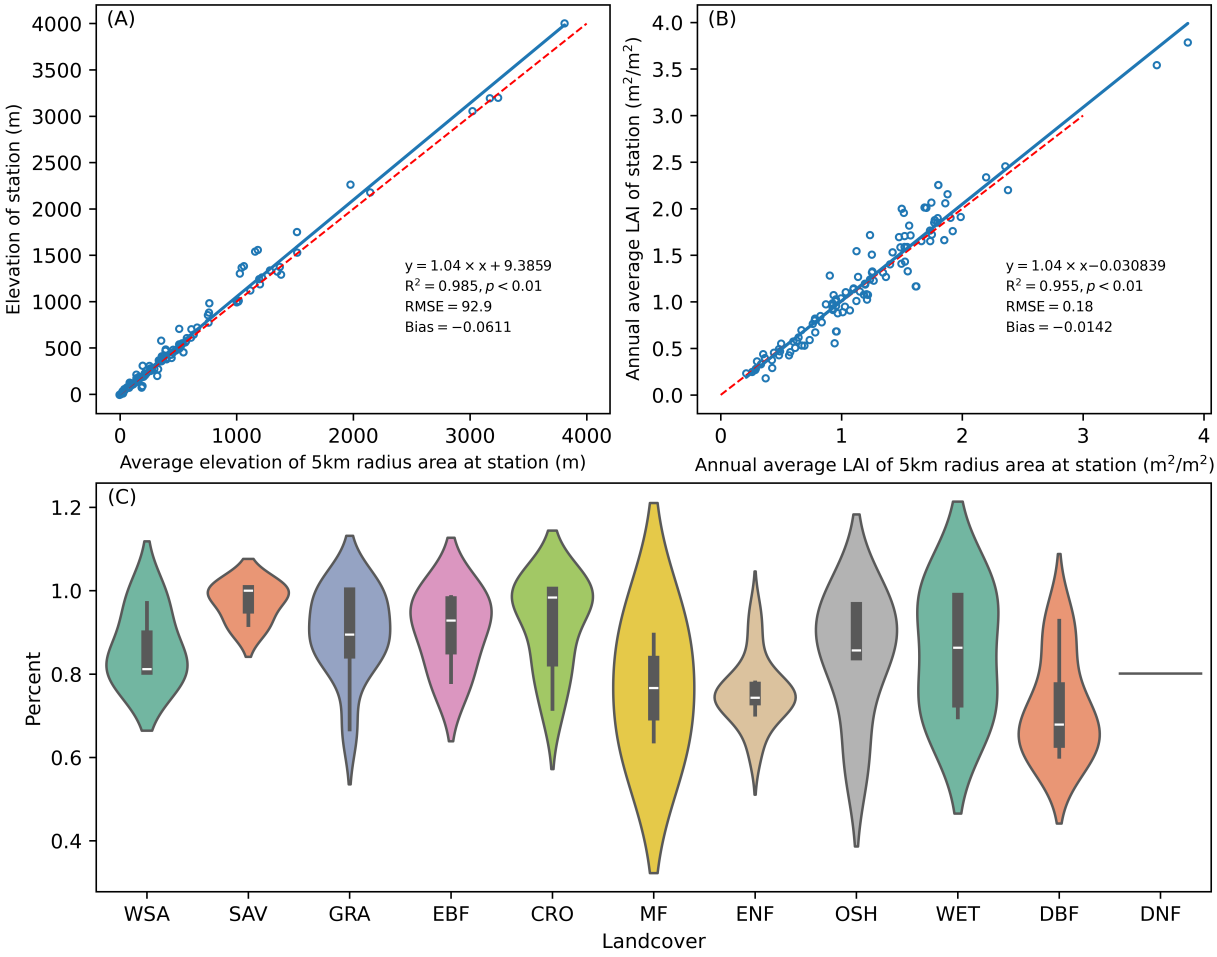

Figure 7. (**A**) Comparison of site elevation and the average elevation within a 5 km radius area of the site. (**B**) Comparison of annual average site LAI and annual average LAI within a 5 km radius of the site. The blue line is the regression line, and the red dashed line is the 1:1 line. The regression equation, correlation coefficients, statistical significance, mean square error, and bias are shown on the bottom. (**C**) The proportion of vegetation types at the site relative to vegetation types within a 5 km radius of the site. WSA: woody savannas; SAV: savannas; GRA: grasslands; EBF: evergreen broadleaf forests; CRO: croplands; MF: mixed forests; ENF: evergreen needleleaf forests; OSH: open shrublands; WET: permanent wetlands; DBF: deciduous broadleaf forests; DNF: deciduous needleleaf forests).

4.2. Drivers of Global GPP Changes from 2000 to 2022

GPP quantifies the carbon uptake of plants through photosynthesis, which is influenced by factors such as temperature, available water, and CO_2 concentration and is crucial in determining the overall productivity of plant ecosystems (Figure 8). Globally, the sensitivity of environmental variables to GPP was assessed and compared with 10 remote sensing models. It was found that the main cause of the increase in GPP was the positive response of plants to increases in atmospheric CO_2 concentration, air temperature, and precipitation, with mean values of 23.9 ± 12.62 PgC year^{-1} 100 ppm^{-1}, 6.655.3 PgC year^{-1} °C^{-1}, and 2.62.03 PgC year^{-1} 100 mm^{-1}, respectively [82]. The C-Fix model evaluated the impact of climatic factors on GPP trends, spanning from 1982 to 2015, revealing that the global average contributions of atmospheric CO_2 concentration, air temperature, and water to the GPP trend were 65.37%, 13.07%, and 11.74%, respectively [83]. Atmospheric CO_2 concentration was a key environmental factor that affected global GPP and made the largest positive contribution to its increase [84].

In this study, we investigated the correlation of global summed GPP with the climate variables of air temperature, atmospheric CO_2 concentration, and precipitation to quantify the total effect of environmental variables on long-term changes in GPP. Over the last two

decades, global trends have shown continuous increases in atmospheric CO_2 concentration, air temperature, and precipitation [85], with increases of 2.19 ppm per year [86,87], 0.0405 °C per year [88], and 0.377 mm per year, respectively. The correlation between GPP and air temperature, atmospheric CO_2 concentration, and precipitation was 0.866, 0.927, and 0.131, respectively (Figure 8). The emission of greenhouse gases such as CO_2 contributed to global warming through the greenhouse effect and led to a prolonged growing season, especially at high and mid-latitudes, resulting in increased GPP [89]. The analysis of global process model results suggested that part of the increase in terrestrial carbon uptake could be attributed to increased vegetation productivity caused by the fertilization effect of elevated atmospheric CO_2 concentrations [90–92]. Adequate precipitation effectively boosted GPP by enhancing soil moisture and plant growth, while excessive precipitation posed the risk of causing flooding, damaging plants, and inhibiting GPP due to altered soil properties.

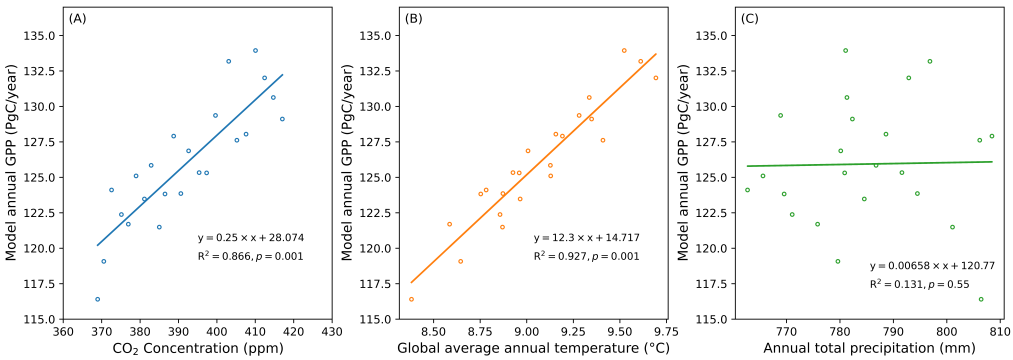

Figure 8. Correlations between global GPP and (**A**) annual mean atmospheric CO_2 concentration, (**B**) global annual mean temperature, and (**C**) global annual precipitation.

Structural equation modeling (SEM) is a significant method for the analysis of ecological data that is capable of quantifying both direct and indirect causal relationships among multiple variables (Figure 9). SEM not only determines the individual path coefficient for each relationship but also assesses the overall model fit to provide a comprehensive understanding of natural systems [67–69]. A structural equation model was developed to explore the impacts of storm frequency on both the structure of kelp forest communities and the complexity of their food webs with a p value = 0.115 [67,68]. The SEM model was used to construct the direct response of species richness to abiotic stress and disturbance and the intervention effect on community biomass [70].

We were able to quantify both the direct and indirect paths of atmospheric CO_2 concentration, air temperature, and precipitation for increasing GPP based on the SEM model (Figure 9). The total effects on GPP change, including the effects of atmospheric CO_2 concentration, air temperature, and precipitation change, were 0.853, 0.75, and −0.144, respectively, when the direct and indirect effects of the latent variables were aggregated (Figure 9A). The increasing concentration of CO_2 altered the surface energy balance and led to climate change, which subsequently affected atmospheric circulation and the global water cycle, changing the temporal and spatial distribution of precipitation [93,94]. The change in CO_2 had not only a positive and direct effect, with an influence coefficient of 0.261, but also a positive and indirect effect, with an influence coefficient of 0.62, on the change in GPP through its positive effect on temperature, as well as a positive and indirect effect, with an influence coefficient of -0.028, on the GPP change through its negative effect on precipitation (Figure 9B).

The EC-LUE model assessed the impact of atmospheric CO_2 concentration on GPP trends, discovering that a 100 ppm^{-1} rise in atmospheric CO_2 concentration significantly boosted the global GPP by 12.31 ± 0.61 PgC [4]. While precipitation made a minor but negative contribution to global GPP, the VPM, VI (Vegetation Indices), TG (Temperature–Greenness), and GR (Greenness–Radiation) models had respective mean values of

-1.4949 PgC year^{-1} 100 mm^{-1}, -0.85859 PgC year^{-1} 100 mm^{-1}, -0.85859 PgC year^{-1} 100 mm^{-1}, and -0.36364 PgC year^{-1} 100 mm^{-1} [82]. The VPM model focuses on radiation and temperature in GPP estimation and neglects precipitation, while the VI and TG models focus on vegetation indices and temperature and indirectly reflect the effects of precipitation. The GR model, which relies heavily on radiation, associates increased precipitation with lower radiation and GPP. The global GPP has a negative impact at the global level but not at the regional level, where the increase in precipitation depends on the climatic characteristics of the region, the water requirements of the ecosystems, and interaction with other relevant environmental variables. At the global scale, an increase in precipitation could lead to cloud thickening and reduced solar radiation, as well as waterlogged soils that limit the oxygen supply to roots, thereby inhibiting plant photosynthesis. At a regional scale, the effects of precipitation on GPP vary depending on the type of vegetation, topography, and soil conditions. GPP changes are influenced primarily by an increase in radiation and temperature at mid- and high latitudes, by changes in moisture conditions at low latitudes, and by fluctuations in both temperature and moisture conditions at high altitudes [95]. Changes in photosynthetically active radiation, relative humidity, and temperature were the primary drivers of the interannual variability in GPP, accounting for 80% in deciduous broadleaf forests and evergreen coniferous forests, 65% in crop plants, and 58% in shrubs [96]. Different plants have different light saturation points and radiation utilization rates, which means that the radiation intensity required to achieve maximum photosynthetic efficiency varies from plant to plant. Temperature affects the activity of key enzymes such as Rubisco, influencing the rate of photosynthesis. Humidity affects the transpiration and stomatal conductance of plants, which, in turn, affect CO_2 uptake and water use efficiency.

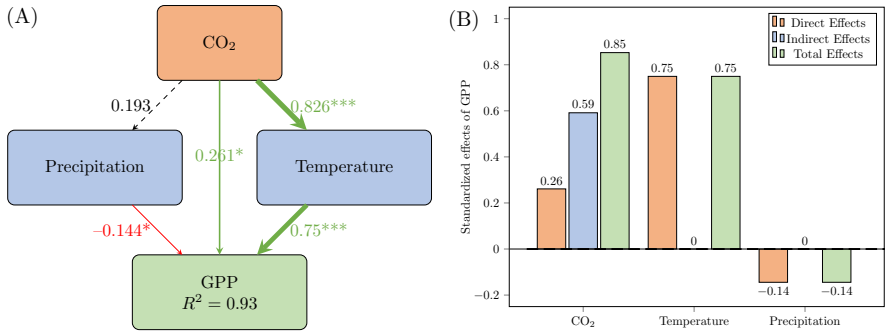

Figure 9. The basic usage of structural equation modeling (SEM) in path analysis with mediation. (**A**) The causal relationships include total effects and their corresponding path coefficients. The acronyms in the models are carbon dioxide (CO_2), air temperature (Temperature), GPP, and Precipitation. * indicates statistical significance ($p < 0.05$), and *** indicates extremely significant ($p < 0.001$). Model fit was assessed using Shipley's test of d separation (Fisher's C = 0.104, df = 2, $p = 0.95$). (**B**) Standardized effects of driving factors (CO_2, Temperature, and Precipitation) on GPP.

5. Conclusions

We estimated global GPP from 2000 to 2022 based on GPU by integrating the Farquhar model for C3 plants and the Collatz model for C4. The proposed model showed strong performance in simulating both spatial and interannual variations in GPP globally. It explained 72.3% of the spatial variation at all validation sites and showed interannual changes consistent with other models. We assessed the contributions of climate factors to GPP trends and found that these environmental variables exhibit substantial long-term changes and contribute significantly to vegetation production on an interannual scale. Atmospheric CO_2 concentration is an important environmental factor that increases global annual GPP according to the SEM model. The model we developed was able to effectively capture temporal and spatial changes in GPP and provides a reliable alternative for long-term estimates of global GPP.

While the Light-Use Efficiency (LUE) model has been widely used to estimate vegetation productivity, it has encountered several limitations, including the failure to account for environmental stressors, inconsistencies in spatial and temporal scales, region-specific parameterization, and the inability to fully capture the dynamic interactions within complex ecosystems [97–100]. Although vegetation index models have been widely used to monitor vegetation condition and productivity, they are limited by their sensitivity to atmospheric conditions, soil background effects, and saturation in densely vegetated areas, which reduces their accuracy in estimating biophysical parameters [2,101]. AI models for estimating gross primary production (GPP) often encounter limitations due to their dependence on the quality and quantity of input data, the complexity of ecosystem processes, and difficulties in generalizing across different biomes, leading to uncertainties in model predictions [102,103]. Ecosystem process-based models for estimating GPP have the advantage of integrating detailed physiological and ecological mechanisms, which enable more accurate predictions of carbon fluxes at different temporal and spatial scales [81,104,105]. Our dataset provides a higher temporal resolution than the Blue Carbon, SiB4, BCC-ESM1, and CNRM-CM6-1 datasets; higher spatial accuracy than CARDAMOM, BCC-ESM1, and CNRM-CM6-1; and a longer temporal span than BEPS, BESS, Blue Carbon, SiB4, SMAP L4, and CARDAMOM.

The proposed model generated a global GPP dataset with a resolution of 10 km, but this moderate spatial resolution led to the loss of important fine-scale details, resulting in an oversimplified representation of heterogeneous landscapes and lower accuracy in detecting small-scale ecological processes and land use changes. We developed the model using parallel computing techniques, including GPUs and multithreading, which significantly enhanced the simulation speed. Users applying this model to simulate global GPP are required to set up the development environment and possess proficiency in computer skills, such as C++ programming standards. These technical demands pose considerable challenges for beginners. Furthermore, since the model was designed for a global scale, recalibration of parameters is necessary to improve simulation accuracy when applying it to smaller-scale GPP simulations.

For future studies, we plan to improve the spatial accuracy of GPP simulation and more accurately reflect the characteristics of surface changes. We plan to further develop the net primary production (NPP) and net ecosystem production (NEP) modules to enable a more comprehensive simulation of the carbon cycle. These improvements are crucial for understanding the dynamics of the carbon cycle in ecosystems and the impact of climate change on vegetation productivity. We also plan to integrate additional variables, optimize computational algorithms, and improve spatial resolution to increase accuracy and efficiency. In addition, developing modular features, creating a user-friendly interface, increasing calibration efforts, and open-sourcing the model would expand its applicability and ensure reliability in different ecosystems and under different climate conditions. We anticipate that these improvements will enable the model to play an important role in broader ecological research and climate policy development.

Author Contributions: M.X. and S.W. designed of the research. S.W. performed literature review. M.X. and S.W. collected the data. M.X., S.W. and L.H. conducted modeling and statistical analysis and made the graphics with supporting advice from X.Z., J.S. and M.X. S.W. wrote the manuscript. M.X., S.W., X.Z. and J.S. edited and improved the manuscript. M.X. provided financial support for this study. All authors have read and agreed to the published version of the manuscript.

Funding: This research was funded by National Key Research and Development Program of China (grant number 2023YFF0805903) and the Natural Science Foundation of Henan (grant number 242300420219).

Data Availability Statement: The proposed GPP model data derived in this study are available at a yearly temporal resolution at https://figshare.com/articles/dataset/Improved_estimate_of_global_gross_primary_production_for_reproducing_its_long-term_variation_1982-2017/8942336/3 (accessed on 28 September 2024). The land type datasets used in this study are MCD12Q1.006 land cover data (https://doi.org/10.5067/MODIS/MCD12Q1.006 (accessed on 8 October 2020)), ERA-Interim meteorological

data (https://www.ecmwf.int/en/forecasts/datasets/browse-reanalysis-datasets (accessed on 12 October 2021)), the FLUXNET2015 dataset (https://fluxnet.org/data/fluxnet2015-dataset/ (accessed on 16 August 2021)), MODIS GPP products (https://doi.org/10.5067/MODIS/MOD17A2H.006 (accessed on 4 December 2019)), BEPS GPP products (https://doi.org/10.12199/nesdc.ecodb.2016YFA0600200.02.001 (accessed on 4 December 2023)), VPM GPP products (https://doi.org/10.1594/PANGAEA.879558 (accessed on 16 August 2023)), Google Earth Engine surface solar radiation downwards products (https://doi.org/10.24381/cds.68d2bb30 (accessed on 16 May 2023)), vegetation CI dataset products (https://doi.org/10.12199/nesdc.ecodb.2016YFA0600200.01.003 (accessed on 16 August 2021)), and the C3 and C4 vegetation dataset products (https://doi.org/10.1029/2001GB001807 (accessed on 16 August 2021)).

Conflicts of Interest: The authors declare no conflicts of interest.

Appendix A. The Structure of the Model

Total radiation at the top of the atmosphere (AT) is the ratio of total downward shortwave radiation (S_t) to extraterrestrial radiation (S_0).

$$AT = S_t / S_0 \tag{A1}$$

$$S_0 = S_c \times cos(\theta) \tag{A2}$$

where θ is the solar zenith angle and S_c is a solar constant (1367 W/m^2).

We estimated the cloudiness fraction (C_f) based on the total incoming shortwave radiation using the following empirical relationship [45]:

$$C_f = \begin{cases} 0 & ,clearsky \\ 1 - \frac{AT - a_s}{b_s} & ,cloudiessfraction \\ 1 & ,fullcloudysky \end{cases} \tag{A3}$$

where a_s is the fraction of extraterrestrial radiation on overcast days and $a_s + b_s$ is the fraction of extraterrestrial radiation on clear days (in this paper, $a_s = 0.25$ and $b_s = 0.5$).

Bristow and Campbell estimated the proportion of total radiant energy from the top of the atmosphere reaching the canopy using the diurnal temperature difference method [106]. Through this proportion, the direct radiation (AT_b) and scattered radiation (AT_d) reaching the canopy can be calculated as follows:

$$AT_b = \lambda AT_c(1 - C_f) \tag{A4}$$

$$AT_d = AT - AT_b \tag{A5}$$

$$AT_c = \max(AT, a_s + b_s) \tag{A6}$$

where λ is the ratio of direct to total radiation for a clear sky (in this paper, $\lambda = 6/7$) and AT_c is the clear-sky transmission factor.

The total downward shortwave radiation (S_t) that reaches the top of the atmosphere is partitioned into incoming direct radiation (S_b) and diffuse radiation (S_d) [44] as follows:

$$S_b = \frac{AT_b}{AT} S_t \tag{A7}$$

$$S_d = \frac{AT_d}{AT} S_t \tag{A8}$$

Appendix A.1. Canopy Radiative Transfer

We applied the two-stream approach to develop a transmission model that accounts for multiple scatterings and reflection in the finite and infinite canopy to better estimate radiant energy inside and outside the canopy [44]. It is assumed that radiation is scattered equally in an upward and downward direction and that the scattering direction is along the same path as the incoming radiation. This model considers incoming radiation to be either transmitted through the canopy, reflected by the canopy, or absorbed by the canopy.

$$\tau = \frac{\tau'(1-(\beta')^2)}{1-(\beta')^2(\tau')^2} \tag{A9}$$

$$\beta = \frac{\beta'(1-(\tau')^2)}{1-((\beta')^2)(\tau')^2} \tag{A10}$$

where τ and β are the corresponding transmission and reflection factors for a finite canopy, respectively, and τ' and β' are the corresponding transmission and reflection factors for an infinitely deep canopy, respectively.

$$\begin{aligned}\tau_d' = {} & (1-\sqrt{1-\alpha}\times G\times LAI)e^{-\sqrt{1-\alpha}\times G\times LAI} \\ & + (\sqrt{1-\alpha}\times G\times LAI)^2 \\ & \times E_i(1,\sqrt{1-\alpha}\times G\times LAI)\end{aligned} \tag{A11}$$

$$\tau_b' = e^{-\sqrt{1-\alpha}K_b LAI} \tag{A12}$$

$$\beta' = \frac{1-\sqrt{1-\alpha}}{1+\sqrt{1-\alpha}} \tag{A13}$$

where α is the leaf-scattering coefficient ($\alpha_b = 0.1$, $\alpha_d = 0.65$). Since the approach for diffuse radiation is just an integral of single-beam components over the hemisphere, the reflection factors for an infinitely deep canopy (β_b' and β_d') are estimated using the same equation.

$$G = \phi_1 + \phi_2 cos\theta \tag{A14}$$

$$\phi_1 = 0.5 - 0.633\chi - 0.33\chi^2 \tag{A15}$$

$$\phi_2 = 0.877(1-2\phi_1) \tag{A16}$$

where G is the leaf orientation factor depending on the solar zenith angle [107] and is an empirical leaf angle distribution parameter ranging from -1 to 1 (-1 for vertical distributed leaves, 0 for a spherical leaf angle distribution with randomly distributed leaves, and 1 for horizontally distributed leaves).

$$K_b = G/cos\theta \tag{A17}$$

where K_b is the extinction coefficient of black leaves.

$$E_i(n,x) = \int_1^\infty \frac{e^{-xt}}{t^n}\,dt \tag{A18}$$

where $E_i(n,x)$ is an exponential integral with n a non-negative integer [47].

Since the exponential integral cannot be computed directly within the GPU, the exponential integral is solved by approximation [108–110] as follows:

$$part1 = \frac{e^{-x}}{2} ln(1+\frac{2}{x}) \tag{A19}$$

$$part2 = e^{-x} ln(1+\frac{1}{x}) \tag{A20}$$

$$E_i(n,x) = \frac{part1+part2}{2} \tag{A21}$$

Appendix A.2. Two-Leaf Model

We adopted the two-leaf model to estimate the radiation absorbed by the canopy, which divides the canopy into shaded and sunlit leaves that receive different components and portions of incoming shortwave radiation [49]. It is assumed that the sunlit leaves

receive both direct and diffuse solar radiation, while shaded leaves absorb diffuse radiation only [48]. We obtained the LAI of shaded and sunlit leaves of the canopy by using the LAI [107].

$$LAI_{sun} = \frac{1}{K_b}(1 - e^{-K_b \times LAI \times CI}) \tag{A22}$$

$$LAI_{shade} = LAI - LAI_sun \tag{A23}$$

where CI is clumping index.

The total solar radiation flux density absorbed by the sunlit leaves in the canopy (AS_{sun}) is the sum of the direct component of direct radiation ($AS_{b,b}$), the scattered component of direct radiation ($AS_{b,s}$), and diffuse radiation (AS_d).

$$AS_{sun} = AS_{b,b} + AS_{b,s} + AS_d \tag{A24}$$

The total solar radiation flux density absorbed by shaded leaves in the canopy (AS_{shade}) is the sum of the scattered component of direct radiation ($AS_{b,s}$) and diffuse radiation (AS_d):

$$AS_{shade} = AS_{b,s} + AS_d \tag{A25}$$

We coupled the canopy radiative transfer model with the two-leaf model to calculate the absorption of different radiation components for sunlit and shaded leaves. The absorbed diffuse radiation (AS_d) is expressed as follows:

$$AS_d = S_d(1 - \tau_d - \beta_d) \tag{A26}$$

The absorbed direct component of direct radiation ($AS_{b,b}$) is expressed as follows:

$$AS_{b,b} = S_b K_b \tag{A27}$$

The absorbed scattered component of direct radiation ($AS_{b,s}$) is expressed as follows:

$$AS_{b,s} = S_b(1 - \tau_b - \beta_b) - AS_{b,b} \tag{A28}$$

Appendix A.3. Stomatal Conductance

In our study, the Ball–Berry–Leuning (BBL) stomatal conductance model was coupled with the photosynthesis process [50]. The stomatal conductance is expressed as follows:

$$g_s = g_0 + g_1 \times \frac{A_n}{(1 + \frac{VPD}{D_0}) \times (C_a - \Gamma^*)} \tag{A29}$$

where A_n is the net leaf CO_2 assimilation rate; VPD is the vapor pressure deficit; C_a is the CO_2 concentration at the leaf surface; Γ^* is the CO_2 compensation point; and g_0, g_1, and D_0 are empirical coefficients, the values of which [111] are presented in Table A1.

Table A1. Parameters for stomatal conductance.

Parameter	Value	Unit	Reference
g_0	7.5		Panek et al., 2001 [111]
g_1	0.01	mol × m^{-2} × s^{-1}	Panek et al., 2001 [111]
D_0	2	Kpa	Panek et al., 2001 [111]

Appendix A.4. Sunrise and Sunset

The times of sunrise and sunset are affected by several factors, including season, geographical location, and the Earth's rotation. Since the Earth's orbit is elliptical, the distance between the Earth and the Sun varies depending on the season. In winter, when

the Earth is farther from the Sun, the Sun rises later and sets earlier, while in summer, the opposite is true. The longitudes of the different regions are different because the globe is a sphere. In the same season, the Sun usually rise earlier and sets later in regions with eastern longitude than in regions with western longitude. As the Earth rotates, the sunrise and sunset times differ between locations on Earth.

$$delta = 23.45 \times sin(\frac{doy - 80}{365} \times 360 \times \frac{\pi}{180}) \times \frac{\pi}{180} \tag{A30}$$

where *delta* is the solar declination and *doy* is the day of the year.

$$cos(\omega) = -tan(Lat \times \frac{\pi}{180}) \times tan(delta) \tag{A31}$$

where ω is the hour angle and *Lat* is the latitude.

Polar day and night occur at high latitudes, which affects the calculation results of radiation flux.

$$beta = \begin{cases} 1 & ,cos(\omega) \geq 1 \\ cos(\omega) & ,-1 < cos(\omega) < 1 \\ -1 & ,cos(\omega) \leq -1 \end{cases} \tag{A32}$$

We can obtain the sunrise and sunset as follows:

$$SunRise = 12 - \frac{arccos(beta) \times \frac{180}{\pi}}{15} \tag{A33}$$

$$SunSet = 12 + \frac{arccos(beta) \times \frac{180}{\pi}}{15} \tag{A34}$$

Appendix A.5. Local Time

Local time is the time observed in a specific locality. All 15 longitudes of the earth are divided into corresponding time zones. Due to the Earth's rotation and the differences in longitude between regions, the local time varies depending on the geographical location.

$$TimeZone = (\frac{Lon + 7.5}{15}) - 1 \tag{A35}$$

$$LocalTime = (timeSers + TimeZone)\%24 \tag{A36}$$

$$LocalTime = \begin{cases} LocalTime + 24 & ,LocalTime < 0 \\ LocalTime & ,LocalTime \geq 0 \end{cases} \tag{A37}$$

where *Lon* is the longitude and *timeSers* is the Greenwich Meridian local time.

Appendix A.6. The Ratios of Photosynthesis in Sunrise and Sunset Time Zones

Sunrise and sunset occur within a time zone, and the proportion of time with sunshine must be calculated so that the radiant flux can be estimated more accurately.

$$TR_1 = TR/2 \tag{A38}$$

$$UpperSunRise = SunRise - TR_1 \tag{A39}$$

$$LowerSunRise = SunRise + TR_1 \tag{A40}$$

$$UpperSunSet = SunSet - TR_1 \tag{A41}$$

$$LowerSunSet = SunSet + TR_1 \tag{A42}$$

where $UpperSunRise$ and $LowerSunRise$ are the upper and lower boundaries of the sunrise time zone, respectively. $UpperSunSet$ and $LowerSunSet$ are the upper and lower boundaries of the sunset time zone, respectively. TR is the temporal resolution.

$$factor = \begin{cases} 0 & ,LT < UpperSunRise || LowerSunSet < LT \\ |LT - SunRise| & ,UpperSunRise < LT < LowerSunRise \\ |LT - SunSet| & ,UpperSunSet < LT < LowerSunSet \\ 1 & ,LowerSunRise < LT < UpperSunSet \end{cases} \quad (A43)$$

where $LT = LocalTime$.

Appendix A.7. Photosynthesis

We divided the vegetation into C3 and C4 plants and calculated the photosynthesis of each pixel based on the ratio of C3 to C4 of each pixel. We used the biochemical photosynthesis model for C3 plants based on Farquhar's model [51] and for C4 plants based on the Collatz's model [52].

The net leaf photosynthesis (A_n) could be modeled as the minimum of three limiting rates after accounting for dark respiration (R_d).

$$A_n = min(A_c, A_j, A_p) - R_d \quad (A44)$$

where A_c is the rate of leaf photosynthesis when the Rubisco carboxylase is limited, which is expressed as follows:

$$A_c = \begin{cases} V_{cmax} \times \frac{C_i - \Gamma^*}{C_i + K_c(1 + O_i/K_o)} & ,\text{for } C3 \\ V_{cmax} & ,\text{for } C4 \end{cases} \quad (A45)$$

where V_{cmax} is the maximum rate of leaf carboxylation; C_i and O_i are the intercellular and atmospheric CO_2 concentrations, respectively; Γ^* is the CO_2 compensation point in the absence of dark respiration; and K_c and K_o are the Michaelis–Menten constants for Rubisco carboxylation and oxygenation, respectively.

A_j is the rate of leaf photosynthesis when light is limited [112], which is expressed as follows:

$$A_j = \begin{cases} J \times \frac{C_i - \Gamma^*}{4C_i + 8\Gamma^*} & ,\text{for } C3 \\ 0.067 \times Q & ,\text{for } C4 \end{cases} \quad (A46)$$

where J is the rate of electron transport and Q is the photosynthetically active photon flux density.

A_p is the rate of photosynthesis when the product is limited for C3 plants and when the PEP carboxylase is limited for C4 plants, which is expressed as follows:

$$A_p = \begin{cases} 0.5 \times V_{cmax} & ,\text{for } C3 \\ k_p \times \frac{C_i}{P_a tm} & ,\text{for } C4 \end{cases} \quad (A47)$$

where k_p is the initial slope of the C4 CO_2 response curve and $P_a tm$ is the atmospheric pressure.

A_c and A_j are also affected by the diffusion constraints, which is expressed as follows:

$$A_{c\ or\ j} = (C_a - C_i) \times G_{CO_2} \quad (A48)$$

where G_{CO_2} is the velocity of CO_2 diffusion from the atmosphere into leaves.

J depends on the photosynthetically active radiation absorbed by the leaf and expressed as follows [112]:

$$\theta J^2 - (\alpha Q + J_{max}) \times J + \alpha Q J_{max} = 0 \quad (A49)$$

where J_{max} is the maximum potential rate of electron transport, θ is the curvature parameter of the light response curve, and α is the quantum yield of electron transport.

The calculation of K_c and K_o varies depending on the temperature threshold of 15 °C, which is expressed as follows:

$$K_o = K_{o25} \times Q_{10,K_o}^{\frac{T-25}{10}} \tag{A50}$$

$$K_c = \begin{cases} K_{o25} \times Q_{10,K_o}^{\frac{T-25}{10}} & \text{, for } T > 15°C \\ \frac{K_{c25} \times (Q_{10,Kc} \times 1.8)^{\frac{T-15}{10}}}{Q_{10,Kc}} & \text{, for } T \leq 15°C \end{cases} \tag{A51}$$

where T is the air temperature.

We further calculated the vapor pressure deficit (VPD) as one of our input variables for the model by using dewpoint temperature and air temperature. The VPD, which is the difference between the saturated vapor pressure and the actual vapor pressure [113], is commonly used to predict leaf stomatal conductance and photosynthesis [50].

$$es = 0.61078 \times e^{\frac{17.27 \times T}{T+237.3}} \tag{A52}$$

$$ea = 0.61078 \times e^{\frac{17.27 \times T_d}{T_d+237.3}} \tag{A53}$$

$$VPD = es - ea \tag{A54}$$

where T_d is the dewpoint temperature.

We used a temperature function and a high-temperature stress function to scale and describe the temperature dependences of V_{cmax}, J_{max}, Γ^*, and R_d [112,114–116].

Appendix A.8. Photosynthesis of C3 Plants

For C3 plants, the equations are expressed as follows:

$$V_{cmax} = V_{cmax25} \times f(T) \times f_H(T) \tag{A55}$$

$$J_{max} = J_{max25} \times f(T) \times f_H(T) \tag{A56}$$

$$R_d = R_{d25} \times f(T) \times f_H(T) \tag{A57}$$

The corresponding temperature function is expressed as follows:

$$f(T) = e^{\frac{\Delta \times (T-298.15)}{298.15 \times R_{gas} \times T}} \tag{A58}$$

$$f_H(T) = \frac{1 + e^{\frac{298.15 \times \Delta S - \Delta H_d}{298.15 \times R_{gas}}}}{1 + e^{\frac{\Delta \times T - \Delta H_d}{R_{gas} \times T}}} \tag{A59}$$

where R_{gas} is the universal gas constant. The values of temperature dependence parameters ΔH_a, ΔH_d, and ΔS are listed in Table A2.

Table A2. Temperature dependence parameters.

Parameter	ΔH_a (J/mol)	ΔH_d (J/mol)	ΔS (J/mol/K)
V_{cmax}	65,330	149,250	485
J_{max}	43,540	152,040	495
R_d	46,390	150,650	490
ω^*	37,830		

$$J_{max25} = 1.97 \times V_{cmax25} \tag{A60}$$

$$R_{d25} = 0.015 \times V_{cmax25} \tag{A61}$$

$$\Gamma_{25}{}^* = 42.75 \tag{A62}$$

where J_{max25}, R_{d25}, and $\Gamma_{25}{}^*$ are the corresponding parameters at 25 °C.

Appendix A.9. Photosynthesis of C4 Plants

For C4 plants, the equations are expressed as follows:

$$V_{cmax} = V_{cmax25} \times \frac{Q_1 0^{\frac{T_k - 298.15}{10}}}{f_H(T) \times f_L(T)} \quad \text{(A63)}$$

$$J_{max} = J_{max25} \times f(T) \times f_H(T) \quad \text{(A64)}$$

$$R_d = R_{d25} \times \frac{Q_1 0^{\frac{T_k - 298.15}{10}}}{f_H(T)} \quad \text{(A65)}$$

$$\Gamma^* = {\Gamma_{25}}^* \times f(T) \quad \text{(A66)}$$

The corresponding temperature function is expressed as follows:

$$f_H(T) = 1 + e^{S_1 \times (T - S_2)} \quad \text{(A67)}$$

$$f_L(T) = 1 + e^{S_3 \times (S_4 - T)} \quad \text{(A68)}$$

The values of S_1, S_2, S_3, and S_4 are listed in Table A3.

$$J_{max25} = 1.97 \times V_{cmax25} \quad \text{(A69)}$$

$$R_{d25} = 0.025 \times V_{cmax25} \quad \text{(A70)}$$

$${\Gamma_{25}}^* = 42.75 \quad \text{(A71)}$$

Table A3. Photosynthesis parameters.

Parameter	Value	Unit	Reference
θ	7.5		Medlyn et al., 2002 [112]
α	0.01	mol × mol^{-1}	Medlyn et al., 2002 [112]
k_p	2		Oleson et al., 2010 [116]
O_i	210	mmol × mol^{-1}	
R_{gas}	8.314	JK^{-1} × mol^{-1}	
K_{o25}	248	mmol × mol^{-1}	Raj et al., 2014 [117]
K_{c25}	404	µmol × mol^{-1}	Raj et al., 2014 [117]
Q_{10,K_o}	1.2		Raj et al., 2014 [117]
Q_{10,K_c}	2.1		Raj et al., 2014 [117]
Q_{10,R_d}	2.0		Raj et al., 2014 [117]
Q_{10}	2.0		Oleson et al., 2010 [116]
$S_1\ for\ C_{cmax}$	0.3	K^{-1}	Oleson et al., 2010 [116]
$S_2\ for\ C_{cmax}$	313.15	K	Oleson et al., 2010 [116]
S_3	0.2	K^{-1}	Oleson et al., 2010 [116]
S_4	288.15	K	Oleson et al., 2010 [116]
$S_1\ for\ R_d$	1.3	K^{-1}	Oleson et al., 2010 [116]
$S_1\ for\ R_d$	328.15	K	Oleson et al., 2010 [116]

Appendix A.10. Photosynthesis of Nitrogen Content

The maximum rate of carboxylation at 25 °C (V_{cmax25}) depends on the leaf nitrogen concentration and specific leaf area, which is expressed as follows:

$$V_{cmax25} = N_a \times F_{LNR} \times F_{NR} \times a_{R25} \quad \text{(A72)}$$

where N_a is the leaf nitrogen concentration, F_{LNR} is the fraction of leaf nitrogen in Rubisco, F_{NR} is the weight proportion of Rubisco relative to its nitrogen content (in this paper, F_{NR} = 7.16), and a_{R25} is the specific activity in Rubisco (in this paper, a_{R25} = 60).

The leaf nitrogen concentration (N_a) is a function of the C/N ratio and specific leaf area, which is expressed as follows:

$$N_a = \frac{1}{CN_l \times SLA} \quad \text{(A73)}$$

where CN_l is the ratio of carbon to nitrogen in the leaf and SLA is the specific leaf area. CN_l, SLA, and F_{LNR} vary depending on the vegetation type, with values listed in Table A4.

Table A4. Photosynthetic parameters for V_{cmax25}.

Type	CN_l	SLA	F_{LNR}
ENF	42	0.012	0.04
EBF	40	0.012	0.035
DNF	25	0.024	0.055
DBF	24	0.03	0.08
MF	32	0.02	0.06
CSH	42	0.012	0.04
OSH	42	0.012	0.04
WSA	25	0.03	0.09
SAV	25	0.03	0.09
GRA	25	0.045	0.12
WET	42	0.012	0.04
CRO	25	0.07	0.41

Appendix B. Information on the Eddy Covariance (EC) Sites

Table A5. Information on flux tower sites used in this study.

Type	Site ID	Latitude	Longitude	Period	RRMSE
CRO	US-Ne2	41.1649	−96.4701	2001–2012	0.3401
CRO	FI-Jok	60.8986	23.5134	2000–2003	0.6459
CRO	US-Twt	38.1087	−121.6531	2009–2014	0.1806
CRO	BE-Lon	50.5516	4.7462	2004–2010 2012–2014	0.0836 0.3704
CRO	DE-RuS	50.8659	6.4471	2011–2014	0.5154
CRO	DE-Kli	50.8931	13.5224	2005–2011	0.4842
CRO	US-Ne1	41.1651	−96.4766	2001–2012	0.2616
CRO	US-CRT	41.6285	−83.3471	2011–2013	0.3251
CRO	US-Ne3	41.1797	−96.4397	2001–2012	0.2955
CRO	CH-Oe2	47.2864	7.7337	2004–2014	0.5637
CRO	DE-Geb	51.0997	10.9146	2001–2014	0.6072
CRO	DE-Seh	50.8706	6.4497	2008–2009	0.4000
DBF	DE-Hai	51.0792	10.4522	2000–2012	0.3928
DBF	DE-Lnf	51.3282	10.3678	2003–2006 2011–2013	0.4970 0.4344
DBF	DK-Sor	55.4859	11.6446	2000–2013	0.3840
DBF	US-Oho	41.5545	−83.8438	2004–2013	0.2627
DBF	FR-Fon	48.4764	2.7801	2005–2014	0.2886
DBF	IT-CA1	42.3804	12.0266	2014–2014	0.4927
DBF	IT-CA3	42.38	12.0222	2014–2014	0.6707
DBF	IT-Col	41.8494	13.5881	2005–2014	0.6592
DBF	IT-PT1	45.2009	9.061	2002–2004	0.9705
DBF	IT-Ro1	42.4081	11.93	2001–2006	0.5207
DBF	IT-Ro2	42.3903	11.9209	2002–2008 2010–2011	0.5568 0.3531
DBF	JP-MBF	44.3869	142.3186	2004–2005	0.4067
DBF	PA-SPn	9.3181	−79.6346	2008–2008	0.3329
DBF	US-Ha1	42.5378	−72.1715	2000–2012	0.1150
DBF	US-MMS	39.3232	−86.4131	2000–2014	0.3791
DBF	CA-Oas	53.6289	−106.1978	2000–2010	0.6749
DBF	US-Wi3	46.6347	−91.0987	2004–2004	0.1962
DBF	US-UMB	45.5598	−84.7138	2000–2014	0.2032
DBF	US-UMd	45.5625	−84.6975	2008–2014	0.2799
DBF	US-WCr	45.8059	−90.0799	2000–2006 2012–2014	0.2877 0.5901

Table A5. *Cont.*

Type	Site ID	Latitude	Longitude	Period	RRMSE
DNF	RU-SkP	62.255	129.168	2012–2014	1.1955
EBF	AU-Whr	−36.6732	145.0294	2012–2014	0.4912
EBF	CN-Din	23.1733	112.5361	2003–2003	0.5219
				2005–2005	0.4910
EBF	GH-Ank	5.2685	−2.6942	2011–2012	0.4864
EBF	AU-Wac	−37.4259	145.1878	2005–2008	0.1021
EBF	AU-Tum	−35.6566	148.1517	2001–2014	0.9606
EBF	AU-Wom	−37.4222	144.0944	2010–2014	0.4957
EBF	AU-Cum	−33.6152	150.7236	2012–2014	0.9677
EBF	FR-Pue	43.7413	3.5957	2001–2014	0.4651
ENF	US-Me5	44.4372	−121.5668	2000–2002	0.4521
ENF	FI-Sod	67.3624	26.6386	2001–2014	0.4508
ENF	FI-Let	60.6418	23.9595	2010–2012	0.5982
ENF	FI-Hyy	61.8474	24.2948	2000–2014	0.6253
ENF	FR-LBr	44.7171	−0.7693	2000–2008	0.6623
ENF	US-Me6	44.3233	−121.6078	2011–2014	0.2973
ENF	US-Prr	65.1237	−147.4876	2010–2014	0.3164
ENF	US-Me3	44.3154	−121.6078	2004–2008	0.1513
ENF	NL-Loo	52.1666	5.7436	2000–2014	0.1057
ENF	IT-Ren	46.5869	11.4337	2002–2003	0.2438
				2005–2013	0.9499
ENF	RU-Fyo	56.4615	32.9221	2000–2014	0.0590
ENF	US-Blo	38.8953	−120.6328	2000–2007	1.5783
ENF	IT-La2	45.9542	11.2853	2001–2001	0.6657
ENF	US-Wi4	46.7393	−91.1663	2002–2005	0.0204
ENF	US-Me2	44.4523	−121.5574	2002–2014	0.0919
ENF	IT-Lav	45.9562	11.2813	2003–2014	0.6185
ENF	US-GLE	41.3665	−106.2399	2005–2014	0.2307
ENF	CN-Qia	26.7414	115.0581	2003–2005	0.2926
ENF	DE-Tha	50.9626	13.5651	2000–2014	0.5088
ENF	CA-NS3	55.9117	−98.3822	2001–2005	0.4440
ENF	US-NR1	40.0329	−105.5464	2000–2014	0.3379
ENF	CA-SF2	54.2539	−105.8775	2003–2004	0.7883
ENF	CA-SF1	54.485	−105.8176	2004–2005	0.7912
ENF	CA-NS2	55.9058	−98.5247	2001–2004	0.5028
ENF	CA-NS4	55.9144	−98.3806	2002–2005	0.7572
ENF	CZ-BK1	49.5021	18.5369	2004–2014	0.2705
ENF	CA-Man	55.8796	−98.4808	2000–2004	0.5992
ENF	CA-Qfo	49.6925	−74.3421	2004–2010	0.7685
ENF	DE-Lkb	49.0996	13.3047	2009–2013	0.5555
ENF	CA-NS5	55.8631	−98.485	2002–2005	0.7947
ENF	CA-NS1	55.8792	−98.4839	2002–2005	0.7684
GRA	AT-Neu	47.1167	11.3175	2002–2012	0.9405
GRA	US-AR1	36.4267	−99.42	2009–2012	1.4371
GRA	US-Wkg	31.7365	−109.9419	2006–2014	0.1482
GRA	RU-Tks	71.5943	128.8878	2012–2014	0.1329
GRA	US-AR2	36.6358	−99.5975	2010–2011	0.1587
GRA	RU-Ha1	54.7252	90.0022	2003–2004	0.1047
GRA	PA-SPs	9.3138	−79.6314	2007–2009	0.0382
GRA	US-Goo	34.2547	−89.8735	2003–2006	0.2912
GRA	CH-Cha	47.2102	8.4104	2005–2014	0.8429
GRA	DE-RuR	50.6219	6.3041	2012–2014	0.3521
GRA	CH-Oe1	47.2858	7.7319	2002–2008	0.5104
GRA	AU-Ync	−34.9893	146.2907	2013–2013	0.1063
GRA	US-SRG	31.7894	−110.8277	2008–2014	0.2094
GRA	DE-Gri	50.95	13.5126	2004–2011	0.4390
GRA	CZ-BK2	49.4944	18.5429	2006–2012	0.3105
GRA	CH-Fru	47.1158	8.5378	2006–2008	0.7539
				2010–2014	1.9716
GRA	CN-Du2	42.0467	116.2836	2007–2008	0.1365
GRA	IT-MBo	46.0147	11.0458	2003–2013	0.6747
GRA	CN-Cng	44.5934	123.5092	2007–2010	0.5325
GRA	AU-DaP	−14.0633	131.3181	2007–2013	0.9532
GRA	CN-HaM	37.37	101.18	2002–2004	0.2041
GRA	AU-Stp	−17.1507	133.3502	2009–2014	0.9670

Table A5. *Cont.*

Type	Site ID	Latitude	Longitude	Period	RRMSE
MF	CA-Gro	48.2167	−82.1556	2003–2013	0.6731
MF	BE-Bra	51.3076	4.5198	2004–2014	0.0282
MF	JP-SMF	35.2617	137.0788	2003–2006	0.2723
MF	BE-Vie	50.3049	5.9981	2000–2014	0.7275
MF	CN-Cha	42.4025	128.0958	2003–2005	0.7002
MF	CH-Lae	47.4783	8.3644	2004–2014	2.0494
MF	US-PFa	45.9459	−90	2000–2014	0.1197
MF	US-Syv	46.2420	−89.3477	2001–2006 2012–2014	0.3828 0.3959
OSH	CA-NS6	55.9167	−98.9644	2001–2005	0.7761
OSH	US-SRC	31.9083	−110.8395	2008–2012	0.0910
OSH	RU-Cok	70.8291	147.4943	2008–2009	0.0062
OSH	CA-NS7	56.6358	−99.9483	2002–2005	0.7375
OSH	ES-LgS	37.0979	−2.9658	2007–2008	0.4493
OSH	CA-SF3	54.0916	−106.0053	2002–2006	0.8128
OSH	US-Whs	31.7438	−110.0522	2008–2014	0.0364
OSH	US-Sta	41.3966	−106.8024	2007–2009	0.0634
SAV	SN-Dhr	15.4028	−15.4322	2012–2013	0.2812
SAV	SD-Dem	13.2829	30.4783	2007–2009	0.2843
SAV	ZA-Kru	−25.0197	31.4969	2010–2011	0.2859
SAV	AU-DaS	−14.1593	131.3881	2011–2014	0.9589
SAV	AU-Dry	−15.2588	132.3706	2008–2014	0.9672
WET	AU-Fog	−12.5452	131.3072	2006–2007	0.9744
WET	US-Tw1	38.1074	−121.6469	2013–2014	0.3446
WET	FI-Lom	67.9972	24.2092	2007–2009	0.5926
WET	US-Atq	70.4696	−157.4089	2004–2008	0.2103
WET	CN-Ha2	37.6086	101.3269	2003–2005	0.2454
WET	CZ-wet	49.0247	14.7704	2006–2014	0.0591
WET	DE-Akm	53.8662	13.6834	2010–2013	0.5076
WET	DE-Spw	51.8922	14.0337	2011–2014	0.4785
WET	US-Los	46.0827	−89.9792	2001–2006	0.3117
WET	US-Ivo	68.4865	−155.7503	2004–2007	0.2463
WSA	AU-How	−12.4943	131.1523	2002–2005 2007–2014	0.9185 0.9785
WSA	AU-Ade	−13.0769	131.1178	2007–2009	0.9185
WSA	US-Ton	38.4309	−120.966	2001–2014	0.5003
WSA	US-SRM	31.8214	−110.8661	2004–2014	0.0726

References

1. Cui, T.; Sun, R.; Qiao, C.; Zhang, Q.; Yu, T.; Liu, G.; Liu, Z. Estimating diurnal courses of gross primary production for maize: A comparison of sun-induced chlorophyll fluorescence, light-use efficiency and process-based models. *Remote Sens.* **2017**, *9*, 1267. [CrossRef]
2. Xiao, X.; Zhang, Q.; Braswell, B.; Urbanski, S.; Boles, S.; Wofsy, S.; Moore, B., III; Ojima, D. Modeling gross primary production of temperate deciduous broadleaf forest using satellite images and climate data. *Remote Sens. Environ.* **2004**, *91*, 256–270. [CrossRef]
3. Zhang, Y.; Xiao, X.; Wu, X.; Zhou, S.; Zhang, G.; Qin, Y.; Dong, J. A global moderate resolution dataset of gross primary production of vegetation for 2000–2016. *Sci. Data* **2017**, *4*, 1–13. [CrossRef] [PubMed]
4. Zheng, Y.; Shen, R.; Wang, Y.; Li, X.; Liu, S.; Liang, S.; Chen, J.M.; Ju, W.; Zhang, L.; Yuan, W. Improved estimate of global gross primary production for reproducing its long-term variation, 1982–2017. *Earth Syst. Sci. Data* **2020**, *12*, 2725–2746. [CrossRef]
5. Robinson, N.P.; Allred, B.W.; Smith, W.K.; Jones, M.O.; Moreno, A.; Erickson, T.A.; Naugle, D.E.; Running, S.W. Terrestrial Primary Production for the Conterminous United States Derived from Landsat 30 m and MODIS 250 m. *Remote Sens. Ecol. Conserv.* **2018**, *4*, 264–280. [CrossRef]
6. Ludwig, J.A.; Reynolds, J.F. *Statistical Ecology: A Primer in Methods and Computing*; John Wiley & Sons: Hoboken, NJ, USA, 1988; Volume 1.
7. Running, S.W.; Coughlan, J.C. A general model of forest ecosystem processes for regional applications I. Hydrologic balance, canopy gas exchange and primary production processes. *Ecol. Model.* **1988**, *42*, 125–154. [CrossRef]
8. Running, S.W.; Hunt, E.R., Jr. Generalization of a forest ecosystem process model for other biomes, BIOME-BCG, and an application for global-scale models. In *Scaling Physiological Processes*; Academic Press: San Diego, CA, USA, 1993. [CrossRef]
9. Potter, C.S.; Randerson, J.T.; Field, C.B.; Matson, P.A.; Vitousek, P.M.; Mooney, H.A.; Klooster, S.A. Terrestrial ecosystem production: A process model based on global satellite and surface data. *Glob. Biogeochem. Cycles* **1993**, *7*, 811–841. [CrossRef]
10. Prince, S.D.; Goward, S.N. Global primary production: A remote sensing approach. *J. Biogeogr.* **1995**, *22*, 815–835. [CrossRef]

11. Running, S.W.; Zhao, M. Daily GPP and Annual NPP (MOD17A2H/A3H) and Year-end Gap- Filled (MOD17A2HGF/A3HGF) Products NASA Earth Observing System MODIS Land Algorithm (For Collection 6) 2019. Available online: https://modis-land.gsfc.nasa.gov/pdf/MOD17UsersGuide2019.pdf (accessed on 28 September 2024).
12. Sasai, T.; Ichii, K.; Yamaguchi, Y.; Nemani, R. Simulating terrestrial carbon fluxes using the new biosphere model "biosphere model integrating eco-physiological and mechanistic approaches using satellite data"(BEAMS). *J. Geophys. Res. Biogeosciences* **2005**, *110*, G01010. [CrossRef]
13. Veroustraete, F.; Sabbe, H.; Eerens, H. Estimation of carbon mass fluxes over Europe using the C-Fix model and Euroflux data. *Remote Sens. Environ.* **2002**, *83*, 376–399. [CrossRef]
14. Bloomfield, K.J.; Stocker, B.D.; Keenan, T.F.; Prentice, I.C. Environmental controls on the light use efficiency of terrestrial gross primary production. *Glob. Chang. Biol.* **2023**, *29*, 1037–1053. [CrossRef] [PubMed]
15. Ryan, E.M.; Ogle, K.; Peltier, D.; Walker, A.P.; De Kauwe, M.G.; Medlyn, B.E.; Williams, D.G.; Parton, W.; Asao, S.; Guenet, B.; et al. Gross primary production responses to warming, elevated CO_2, and irrigation: Quantifying the drivers of ecosystem physiology in a semiarid grassland. *Glob. Chang. Biol.* **2017**, *23*, 3092–3106. [CrossRef] [PubMed]
16. Turner, D.P.; Ritts, W.D.; Cohen, W.B.; Maeirsperger, T.K.; Gower, S.T.; Kirschbaum, A.A.; Running, S.W.; Zhao, M.; Wofsy, S.C.; Dunn, A.L. Site-level evaluation of satellite-based global terrestrial gross primary production and net primary production monitoring. *Glob. Chang. Biol.* **2005**, *11*, 666–684. [CrossRef]
17. Still, C.J.; Berry, J.A.; Collatz, G.J.; DeFries, R.S. Global distribution of C3 and C4 vegetation: Carbon cycle implications. *Glob. Biogeochem. Cycles* **2003**, *17*, 6-1–6-14. [CrossRef]
18. Still, C.; Berry, J.; Ribas-Carbo, M.; Helliker, B. The contribution of C3 and C4 plants to the carbon cycle of a tallgrass prairie: An isotopic approach. *Oecologia* **2003**, *136*, 347–359. [CrossRef]
19. Shimoda, S.; Murayama, S.; Mo, W.; Oikawa, T. Seasonal contribution of C3 and C4 species to ecosystem respiration and photosynthesis estimated from isotopic measurements of atmospheric CO_2 at a grassland in Japan. *Agric. For. Meteorol.* **2009**, *149*, 603–613. [CrossRef]
20. Collatz, G.; Berry, J.; Clark, J. Effects of Climate and Atmospheric CO2 Partial Pressure on the Global Distribution of C-4 Grasses: Present, Past, and Future. *Oecologia* **1998**, *114*, 441–454. [CrossRef]
21. Shimoda, S.; Mo, W.; Oikawa, T. The Effects of Characteristics of Asian Monsoon Climate on Interannual CO_2 Exchange in a Humid Temperate C3/C4 Co-occurring Grassland. *SOLA* **2005**, *1*, 169–172. [CrossRef]
22. Kjelgaard, J.; Heilman, J.; McInnes, K.; Owens, M.; Kamps, R. Carbon dioxide exchange in a subtropical, mixed C3/C4 grassland on the Edwards Plateau, Texas. *Agric. For. Meteorol.* **2008**, *148*, 953–963. [CrossRef]
23. Luo, X.; Keenan, T.F.; Chen, J.M.; Croft, H.; Colin Prentice, I.; Smith, N.G.; Walker, A.P.; Wang, H.; Wang, R.; Xu, C. Global variation in the fraction of leaf nitrogen allocated to photosynthesis. *Nat. Commun.* **2021**, *12*, 4866. [CrossRef]
24. Walker, A.P.; Quaife, T.; Van Bodegom, P.M.; De Kauwe, M.G.; Keenan, T.F.; Joiner, J.; Lomas, M.R.; MacBean, N.; Xu, C.; Yang, X. The impact of alternative trait-scaling hypotheses for the maximum photosynthetic carboxylation rate (Vcmax) on global gross primary production. *New Phytol.* **2017**, *215*, 1370–1386. [CrossRef] [PubMed]
25. Ju, W.M.; Zhou, Y.L. Global Daily GPP Simulation Data Products from 1981 to 2019. 2021. Available online: http://www.nesdc.org.cn/sdo/detail?id=612f42ee7e28172cbed3d809 (accessed on 22 March 2024).
26. Li, B.; Ryu, Y.; Jiang, C.; Dechant, B.; Liu, J.; Yan, Y.; Li, X. BESSv2.0: A Satellite-Based and Coupled-Process Model for Quantifying Long-Term Global Land–Atmosphere Fluxes. *Remote Sens. Environ.* **2023**, *295*, 113696. [CrossRef]
27. Steve R. MODIS/Terra Gross Primary Productivity 8-Day L4 Global 500m SIN Grid V061. 2021. Available online: https://lpdaac.usgs.gov/products/mod17a2hv061/ (accessed on 22 March 2022).
28. Yanlian, Z. A Data-driven Upscale Product of Global Gross Primary Production, Net Ecosystem Exchange and Ecosystem Respiration. 2020. Available online: https://www.nies.go.jp/doi/10.17595/20200227.001-e.html (accessed on 4 September 2024).
29. Wild, B.; Teubner, I.; Moesinger, L.; Zotta, R.M.; Forkel, M.; van der Schalie, R.; Sitch, S.; Dorigo, W. VODCA2GPP—A New, Global, Long-Term (1988–2020) Gross Primary Production Dataset from Microwave Remote Sensing. *Earth Syst. Sci. Data* **2022**, *14*, 1063–1085. [CrossRef]
30. Liang, S.; Cheng, J.; Jia, K.; Jiang, B.; Liu, Q.; Xiao, Z.; Yao, Y.; Yuan, W.; Zhang, X.; Zhao, X. The Global Land Surface Satellite (GLASS) Product Suite. *Bull. Am. Meteorol. Soc.* **2021**, *102*, E323–E337. [CrossRef]
31. Joiner, J.; Yoshida, Y.; Koehler, P.; Frankenberg, C.; Parazoo, N.C. L2 Daily Solar-Induced Fluorescence (SIF) from ERS-2 GOME, 1995–2003. *ORNL DAAC* **2019**. [CrossRef]
32. Wu, D.; Lin, J.C. *Urban Biogenic CO_2 Fluxes: GPP, Reco and NEE Estimates from SMUrF, 2010–2019*; ORNL DAAC: Oak Ridge, TN, USA, 2021.
33. Haynes, K.D.; Baker, I.T.; Denning, A.S. *SiB4 Modeled Global 0.5-Degree Monthly Carbon Fluxes and Pools, 2000–2018*; ORNL DAAC: Oak Ridge, TN, USA, 2021.
34. Kimball, J.S.; Jones, L.A.; Kundig, T.; Reichle, R. *SMAP L4 Global Daily 9 Km EASE-Grid Carbon Net Ecosystem Exchange*; NSIDC: Boulder, CO, USA, 2021; Volume 6.
35. Yang, Y.; Saatchi, S.S. CMS: Terrestrial Carbon Stocks, Emissions, and Fluxes for Conterminous US, 2001–2016. ORNL DAAC 2021. Available online: https://daac.ornl.gov/cgi-bin/dsviewer.pl?ds_id=1837 (accessed on 4 September 2023) .

36. Wang, S.; Zhang, Y. Long-Term (1982–2018) Global Gross Primary Production Dataset Based on NIRv. A Big Earth Data Platform for Three Poles. 2020. Available online: https://figshare.com/articles/dataset/Long-term_1982-2018_global_gross_primary_production_dataset_based_on_NIRv/12981977/2 (accessed on 4 September 2023).
37. Chen, Z.; Nong, X.; Zang, C.; Ou, W.; Qiu, L. Evolution of Evapotranspiration in the Context of Land Cover/Climate Change in the Han River Catchment of China. *Hydrol. Process.* **2024**, *38*, e15265. [CrossRef]
38. Zhang, Y. PML_V2 Global Evapotranspiration and Gross Primary Production (2002.07–2019.08). National Tibetan Plateau Data Center 2020; Volume 10. Available online: https://cstr.cn/18406.11.Geogra.tpdc.270251 (accessed on 4 September 2023).
39. Wu, T.; Zhang, F.; Zhang, J.; Jie, W.; Zhang, Y.; Wu, F.; Li, L.; Yan, J.; Liu, X.; Lu, X.; et al. Beijing Climate Center Earth System Model Version 1 (BCC-ESM1): Model Description and Evaluation of Aerosol Simulations. *Geosci. Model Dev.* **2020**, *13*, 977–1005. [CrossRef]
40. Program, F. Global Vegetation Productivity Monthly Data Obtained by CNRM-CM6-1 Mode of CMIP6 (1850–2014). National Tibetan Plateau/Third Pole Environment Data Center. 2019. Available online: https://data.tpdc.ac.cn/en/data/30d6b383-7349-40fd-9c13-8a3c6c02d7e4/ (accessed on 28 September 2024).
41. Zhang, Y.; Joiner, J.; Alemohammad, S.H.; Zhou, S.; Gentine, P. A Global Spatially Contiguous Solar-Induced Fluorescence (CSIF) Dataset Using Neural Networks. *Biogeosciences* **2018**, *15*, 5779–5800. [CrossRef]
42. Wang, J.; Sun, R.; Zhang, H.; Xiao, Z.; Zhu, A.; Wang, M.; Yu, T.; Xiang, K. New Global MuSyQ GPP/NPP Remote Sensing Products from 1981 to 2018. *IEEE J. Sel. Top. Appl. Earth Obs. Remote. Sens.* **2021**, *14*, 5596–5612. [CrossRef]
43. Feagin, R.A.; Forbrich, I.; Huff, T.P.; Barr, J.G.; Ruiz-Plancarte, J.; Fuentes, J.D.; Najjar, R.G.; Vargas, R.; Vazquez-Lule, A.; Windham-Myers, L. Gross Primary Production Maps of Tidal Wetlands across Conterminous USA, 2000–2019. ORNL DAAC 2020. Available online: https://daac.ornl.gov/cgi-bin/dsviewer.pl?ds_id=1792 (accessed on 4 September 2023).
44. Mahat, V.; Tarboton, D.G. Canopy radiation transmission for an energy balance snowmelt model. *Water Resour. Res.* **2012**, *48*, 10438. [CrossRef]
45. Shuttleworth, W.J. Evaporation. 1979. Available online: https://nora.nerc.ac.uk/id/eprint/5783/1/IH_056.pdf (accessed on 28 September 2024).
46. Shang, H. Mapping Global Gross Primary Productivity on the Google Earth Engine Platform–Developing and Applying an Improved Process-Based Ecosystem Model. Ph.D. Thesis, The State University of New Jersey, School of Graduate Studies, Rutgers, NJ, USA, 2023.
47. Nijssen, B.; Lettenmaier, D.P. A simplified approach for predicting shortwave radiation transfer through boreal forest canopies. *J. Geophys. Res. Atmos.* **1999**, *104*, 27859–27868. [CrossRef]
48. Spitters, C.; Toussaint, H.; Goudriaan, J. Separating the diffuse and direct component of global radiation and its implications for modeling canopy photosynthesis Part I. Components of incoming radiation. *Agric. For. Meteorol.* **1986**, *38*, 217–229. [CrossRef]
49. Wang, Y.P.; Leuning, R. A two-leaf model for canopy conductance, photosynthesis and partitioning of available energy I: Model description and comparison with a multi-layered model. *Agric. For. Meteorol.* **1998**, *91*, 89–111. [CrossRef]
50. Leuning, R. A critical appraisal of a combined stomatal-photosynthesis model for C3 plants. *Plant Cell Environ.* **1995**, *18*, 339–355. [CrossRef]
51. Farquhar, G.D.; Von Caemmerer, S.; Berry, J.A. A biochemical model of photosynthetic CO2 assimilation in leaves of C3 species. *Planta* **1980**, *149*, 78–90. [CrossRef]
52. Collatz, G.J.; Miquel, R.C.; Berry, J.A. Coupled Photosynthesis-Stomatal Conductance Model for Leaves of C4 Plants. *Aust. J. Plant Physiol.* **1992**, *19*, 519–538. [CrossRef]
53. Rogers, A. The use and misuse of Vmax in Earth System Models. *Photosynth Res.* **2014**, *119*, 15–29. [CrossRef]
54. Fang, H.; Wei, S. The global clumping index dataset at 8-day temporal resolution and 500- metres spatial resolution from 2001 to 2019. 2021. Available online: http://www.nesdc.org.cn/sdo/detail?id=60fd0a417e28176012d3a71a (accessed on 28 September 2024).
55. Balsamo, G.; Albergel, C.; Beljaars, A.; Boussetta, S.; Brun, E.; Cloke, H.; Dee, D.; Dutra, E.; Muñoz-Sabater, J.; Pappenberger, F. ERA-Interim/Land: A global land surface reanalysis data set. *Hydrol. Earth Syst. Sci.* **2015**, *19*, 389. [CrossRef]
56. Muñoz Sabater, J. ERA5-Land Monthly Averaged Data from 1981 to Present. 2019. Available online: https://cds.climate.copernicus.eu/datasets/reanalysis-era5-land-monthly-means?tab=overview (accessed on 6 September 2023).
57. Barnes, W.L.; Xiong, X.; Salomonson, V.V. Status of terra MODIS and aqua MODIS. *Adv. Space Res.* **2003**, *32*, 2099–2106. [CrossRef]
58. Dee, D.P.; Uppala, S.M.; Simmons, A.J.; Berrisford, P.; Poli, P.; Kobayashi, S.; Andrae, U.; Balmaseda, M.A.; Balsamo, G.; Bauer, d.P. The ERA-Interim reanalysis: Configuration and performance of the data assimilation system. *Q. J. R. Meteorol. Soc.* **2011**, *137*, 553–597. [CrossRef]
59. Gorelick, N.; Hancher, M.; Dixon, M.; Ilyushchenko, S.; Thau, D.; Moore, R. Google Earth Engine: Planetary-scale geospatial analysis for everyone. *Remote Sens. Environ.* **2017**, *202*, 18–27. [CrossRef]
60. Kennedy, R.; Yang, Z.; Gorelick, N.; Braaten, J.; Cavalcante, L.; Cohen, W.; Healey, S. Implementation of the LandTrendr Algorithm on Google Earth Engine. *Remote Sens.* **2018**, *10*, 691. [CrossRef]
61. Justice, C.O.; Townshend, J.R.G.; Vermote, E.F.; Masuoka, E.; Wolfe, R.E.; Saleous, N.; Roy, D.P.; Morisette, J. An overview of MODIS Land data processing and product status. *Remote Sens. Environ.* **2002**, *83*, 3–15. [CrossRef]
62. Ma, B.; Xu, M. Identifying Outliers of the MODIS Leaf Area Index Data by Including Temporal Patterns in Post-Processing. *Remote Sens.* **2023**, *15*, 5042. [CrossRef]

63. Wang, S.; Xu, M.; Zhang, X.; Wang, Y. Fitting Nonlinear Equations with the Levenberg–Marquardt Method on Google Earth Engine. *Remote Sens.* **2022**, *14*, 2055. [CrossRef]
64. Wei, S.; Fang, H. Estimation of canopy clumping index from MISR and MODIS sensors using the normalized difference hotspot and darkspot (NDHD) method: The influence of BRDF models and solar zenith angle. *Remote Sens. Environ.* **2016**, *187*, 476–491. [CrossRef]
65. Wei, S.; Fang, H.; Schaaf, C.B.; He, L.; Chen, J.M. Global 500 m clumping index product derived from MODIS BRDF data (2001–2017). *Remote Sens. Environ.* **2019**, *232*, 111296. [CrossRef]
66. R Core Team, R. *R: A Language and Environment for Statistical Computing*; R Core Team: New York, NY, USA, 2013.
67. Lefcheck, J.S. piecewiseSEM: Piecewise structural equation modelling in r for ecology, evolution, and systematics. *Methods Ecol. Evol.* **2016**, *7*, 573–579. [CrossRef]
68. Shi, Y.F.; Shi, S.H.; Huang, X.M. The application of structural equation modeling in ecology based on R. *Chin. J. Ecol.* **2022**, *41*, 1015. [CrossRef]
69. Fan, Y.; Chen, J.; Shirkey, G.; John, R.; Wu, S.R.; Park, H.; Shao, C. Applications of structural equation modeling (SEM) in ecological studies: An updated review. *Ecol. Process.* **2016**, *5*, 1–12. [CrossRef]
70. Grace, J.B.; Anderson, T.M.; Olff, H.; Scheiner, S.M. On the specification of structural equation models for ecological systems. *Ecol. Monogr.* **2010**, *80*, 67–87. [CrossRef]
71. Chen, J.M.; Ju, W.; Ciais, P.; Viovy, N.; Liu, R.; Liu, Y.; Lu, X. Vegetation structural change since 1981 significantly enhanced the terrestrial carbon sink. *Nat. Commun.* **2019**, *10*, 1–7. [CrossRef] [PubMed]
72. He, Q.; Ju, W.; Dai, S.; He, W.; Song, L.; Wang, S.; Li, X.; Mao, G. Drought risk of global terrestrial gross primary productivity over the last 40 years detected by a remote sensing-driven process model. *J. Geophys. Res. Biogeosciences* **2021**, *126*, e2020JG005944. [CrossRef]
73. Liu, Y.; Zhou, Y.; Ju, W.; Wang, S.; Wu, X.; He, M.; Zhu, G. Impacts of droughts on carbon sequestration by China's terrestrial ecosystems from 2000 to 2011. *Biogeosciences* **2014**, *11*, 2583–2599. [CrossRef]
74. Tagesson, T.; Tian, F.; Schurgers, G.; Horion, S.; Scholes, R.; Ahlström, A.; Ardö, J.; Moreno, A.; Madani, N.; Olin, S.; et al. A physiology-based Earth observation model indicates stagnation in the global gross primary production during recent decades. *Glob. Chang. Biol.* **2021**, *27*, 836–854. [CrossRef]
75. Baldocchi, D.D. Assessing the Eddy Covariance Technique for Evaluating Carbon Dioxide Exchange Rates of Ecosystems: Past, Present and Future. *Glob. Chang. Biol.* **2003**, *9*, 479–492. [CrossRef]
76. Xiao, J.; Davis, K.J.; Urban, N.M.; Keller, K.; Saliendra, N.Z. Upscaling Carbon Fluxes from Towers to the Regional Scale: Influence of Parameter Variability and Land Cover Representation on Regional Flux Estimates. *J. Geophys. Res. Biogeosciences* **2011**, *116*, e2011JG001764. [CrossRef]
77. Stoy, P.C.; Mauder, M.; Foken, T.; Marcolla, B.; Boegh, E.; Ibrom, A.; Arain, M.A.; Arneth, A.; Aurela, M.; Bernhofer, C. A Data-Driven Analysis of Energy Balance Closure across FLUXNET Research Sites: The Role of Landscape Scale Heterogeneity. *Agric. For. Meteorol.* **2013**, *171*, 137–152. [CrossRef]
78. Reichstein, M.; Falge, E.; Baldocchi, D.; Papale, D.; Aubinet, M.; Berbigier, P.; Bernhofer, C.; Buchmann, N.; Gilmanov, T.; Granier, A. On the Separation of Net Ecosystem Exchange into Assimilation and Ecosystem Respiration: Review and Improved Algorithm. *Glob. Chang. Biol.* **2005**, *11*, 1424–1439. [CrossRef]
79. Xiao, J.; Ollinger, S.V.; Frolking, S.; Hurtt, G.C.; Hollinger, D.Y.; Davis, K.J.; Pan, Y.; Zhang, X.; Deng, F.; Chen, J. Data-Driven Diagnostics of Terrestrial Carbon Dynamics over North America. *Agric. For. Meteorol.* **2014**, *197*, 142–157. [CrossRef]
80. Jung, M.; Reichstein, M.; Margolis, H.A.; Cescatti, A.; Richardson, A.D.; Arain, M.A.; Arneth, A.; Bernhofer, C.; Bonal, D.; Chen, J. Global Patterns of Land-atmosphere Fluxes of Carbon Dioxide, Latent Heat, and Sensible Heat Derived from Eddy Covariance, Satellite, and Meteorological Observations. *J. Geophys. Res. Biogeosciences* **2011**, *116*, e2011JG001715. [CrossRef]
81. Beer, C.; Reichstein, M.; Tomelleri, E.; Ciais, P.; Jung, M.; Carvalhais, N.; Rödenbeck, C.; Arain, M.A.; Baldocchi, D.; Bonan, G.B. Terrestrial Gross Carbon Dioxide Uptake: Global Distribution and Covariation with Climate. *Science* **2010**, *329*, 834–838. [CrossRef] [PubMed]
82. Sun, Z.; Wang, X.; Zhang, X.; Tani, H.; Guo, E.; Yin, S.; Zhang, T. Evaluating and comparing remote sensing terrestrial GPP models for their response to climate variability and CO2 trends. *Sci. Total Environ.* **2019**, *668*, 696–713. [CrossRef] [PubMed]
83. Sun, Z.; Wang, X.; Yamamoto, H.; Tani, H.; Zhong, G.; Yin, S.; Guo, E. Spatial pattern of GPP variations in terrestrial ecosystems and its drivers: Climatic factors, CO2 concentration and land-cover change, 1982–2015. *Ecol. Inform.* **2018**, *46*, 156–165. [CrossRef]
84. Chen, Y.; Zhu, Z.; Zhao, W.; Li, M.; Cao, S.; Zheng, Y.; Tian, F.; Myneni, R.B. The direct and indirect effects of the environmental factors on global terrestrial gross primary productivity over the past four decades. *Environ. Res. Lett.* **2023**, *19*, 014052. [CrossRef]
85. Piao, S.; Wang, X.; Wang, K.; Li, X.; Bastos, A.; Canadell, J.G.; Ciais, P.; Friedlingstein, P.; Sitch, S. Interannual variation of terrestrial carbon cycle: Issues and perspectives. *Glob. Chang. Biol.* **2020**, *26*, 300–318. [CrossRef]
86. Lan, X.; Tans, P.; Thoning, K.W. Trends in Globally-Averaged CO2 Determined from NOAA Global Monitoring Laboratory Measurements. 2024. Available online: https://gml.noaa.gov/ccgg/trends/global.html?doi=10.15138/9n0h-zh07 (accessed on 23 February 2024).
87. Masarie, K.A.; Tans, P.P. Extension and integration of atmospheric carbon dioxide data into a globally consistent measurement record. *J. Geophys. Res. Atmos.* **1995**, *100*, 11593–11610. [CrossRef]

88. Change, N.G.C. Global Surface Temperature | NASA Global Climate Change. 2024. Available online: https://climate.nasa.gov/vital-signs/global-temperature/?intent=121 (accessed on 28 September 2024).
89. Anderson, T.R.; Hawkins, E.; Jones, P.D. CO2, the greenhouse effect and global warming: From the pioneering work of Arrhenius and Callendar to today's Earth System Models. *Endeavour* **2016**, *40*, 178–187. [CrossRef]
90. Norby, R.J.; Wullschleger, S.D.; Gunderson, C.A.; Johnson, D.W.; Ceulemans, R. Tree responses to rising CO2 in field experiments: Implications for the future forest. *Plant Cell Environ.* **1999**, *22*, 683–714. [CrossRef]
91. Schimel, D.; Stephens, B.B.; Fisher, J.B. Effect of increasing CO2 on the terrestrial carbon cycle. *Proc. Natl. Acad. Sci. USA* **2015**, *112*, 436–441. [CrossRef]
92. Wang, S.; Zhang, Y.; Ju, W.; Chen, J.M.; Ciais, P.; Cescatti, A.; Sardans, J.; Janssens, I.A.; Wu, M.; Berry, J.A.; et al. Recent global decline of CO2 fertilization effects on vegetation photosynthesis. *Science* **2020**, *370*, 1295–1300. [CrossRef] [PubMed]
93. Zhang, S.Z.; Zhu, X.F.; Liu, T.T.; Xu, K.; Guo, R. Response of Gross Primary Production to Drought under Climate Change in Different Vegetation Regions of China. *Acta Ecol. Sin.* **2022**, *42*, 3429–3440. [CrossRef]
94. Knutson, T.R.; Delworth, T.L.; Dixon, K.W.; Stouffer, R.J. Model Assessment of Regional Surface Temperature Trends (1949–1997). *J. Geophys. Res. Atmos.* **1999**, *104*, 30981–30996. [CrossRef]
95. Available online: https://www.sciencedirect.com/science/article/abs/pii/S1574954118300219?via%3Dihub (accessed on 28 September 2024).
96. Xixi,Y.; Xu, Y.; Hao, Z.; Yimian, M.; Chenguang, T.; Yang, C.; Yadong, L. Interannual variability of gross primary productivity at global FLUXNET sites and its driving factors. *Trans. Atmos. Sci.* **2021**, *43*, 1106–1114. [CrossRef]
97. Turner, D.P.; Urbanski, S.; Bremer, D.; Wofsy, S.C.; Meyers, T.; Gower, S.T.; Gregory, M. A Cross-biome Comparison of Daily Light Use Efficiency for Gross Primary Production. *Glob. Chang. Biol.* **2003**, *9*, 383–395. [CrossRef]
98. Yuan, W.; Liu, S.; Yu, G.; Bonnefond, J.M.; Chen, J.; Davis, K.; Desai, A.R.; Goldstein, A.H.; Gianelle, D.; Rossi, F. Global Estimates of Evapotranspiration and Gross Primary Production Based on MODIS and Global Meteorology Data. *Remote Sens. Environ.* **2010**, *114*, 1416–1431. [CrossRef]
99. Sims, D.A.; Rahman, A.F.; Cordova, V.D.; El-Masri, B.Z.; Baldocchi, D.D.; Bolstad, P.V.; Flanagan, L.B.; Goldstein, A.H.; Hollinger, D.Y.; Misson, L. A New Model of Gross Primary Productivity for North American Ecosystems Based Solely on the Enhanced Vegetation Index and Land Surface Temperature from MODIS. *Remote Sens. Environ.* **2008**, *112*, 1633–1646. [CrossRef]
100. Heinsch, F.A.; Zhao, M.; Running, S.W.; Kimball, J.S.; Nemani, R.R.; Davis, K.J.; Bolstad, P.V.; Cook, B.D.; Desai, A.R.; Ricciuto, D.M. Evaluation of Remote Sensing Based Terrestrial Productivity from MODIS Using Regional Tower Eddy Flux Network Observations. *IEEE Trans. Geosci. Remote Sens.* **2006**, *44*, 1908–1925. [CrossRef]
101. Huete, A.; Didan, K.; Miura, T.; Rodriguez, E.P.; Gao, X.; Ferreira, L.G. Overview of the Radiometric and Biophysical Performance of the MODIS Vegetation Indices. *Remote Sens. Environ.* **2002**, *83*, 195–213. [CrossRef]
102. Reichstein, M.; Camps-Valls, G.; Stevens, B.; Jung, M.; Denzler, J.; Carvalhais, N.; Prabhat, F. Deep Learning and Process Understanding for Data-Driven Earth System Science. *Nature* **2019**, *566*, 195–204. [CrossRef]
103. Tramontana, G.; Jung, M.; Schwalm, C.R.; Ichii, K.; Camps-Valls, G.; Ráduly, B.; Reichstein, M.; Arain, M.A.; Cescatti, A.; Kiely, G. Predicting Carbon Dioxide and Energy Fluxes across Global FLUXNET Sites with Regression Algorithms. *Biogeosciences* **2016**, *13*, 4291–4313. [CrossRef]
104. Sitch, S.; Huntingford, C.; Gedney, N.; Levy, P.E.; Lomas, M.; Piao, S.L.; Betts, R.; Ciais, P.; Cox, P.; Friedlingstein, P. Evaluation of the Terrestrial Carbon Cycle, Future Plant Geography and Climate-carbon Cycle Feedbacks Using Five Dynamic Global Vegetation Models (DGVMs). *Glob. Chang. Biol.* **2008**, *14*, 2015–2039. [CrossRef]
105. Fisher, J.B.; Sikka, M.; Oechel, W.C.; Huntzinger, D.N.; Melton, J.R.; Koven, C.D.; Ahlström, A.; Arain, M.A.; Baker, I.; Chen, J.M. Carbon Cycle Uncertainty in the Alaskan Arctic. *Biogeosciences* **2014**, *11*, 4271–4288. [CrossRef]
106. Bristow, K.L.; Campbell, G.S. On the relationship between incoming solar radiation and daily maximum and minimum temperature. *Agric. For. Meteorol.* **1984**, *31*, 159–166. [CrossRef]
107. Dai, Y.; Dickinson, R.E.; Wang, Y.P. A Two Big Leaf Model for Canopy Temperature, Photosynthesis, and Stomatal Conductance. *J. Clim.* **2004**, *17*, 2281–2299. [CrossRef]
108. Press, W.H.; Vetterling, W.T.; Teukolsky, S.A.; Flannery, B.P. *Numerical Recipes Example Book*; Cambridge University Press: Cambridge, UK, 1992.
109. Chandrasekhar, S. *Radiative Transfer*; Courier Corporation: North Chelmsford, MA, USA, 2013.
110. Abramowitz, M.; Stegun, I.A.; Romer, R.H. *Handbook of Mathematical Functions with Formulas, Graphs, and Mathematical Tables*; American Association of Physics Teachers: College Park, MD, USA, 1988.
111. Panek, J.A.; Goldstein, A.H. A controlled field experiment on the relation between drought stress, photosynthesis and stomatal conductance: Implications for carbon storage and ozone deposition. *Tree Physiol.* **2001**, *21*, 337–344. [CrossRef]
112. Medlyn, B.E.; Dreyer, E.; Ellsworth, D.; Forstreuter, M.; Harley, P.C.; Kirschbaum, M.U.F.; Le Roux, X.; Montpied, P.; Strassemeyer, J.; Walcroft, A. Temperature response of parameters of a biochemically based model of photosynthesis. II. A review of experimental data. *Plant Cell Environ.* **2002**, *25*, 1167–1179. [CrossRef]
113. Yoder, R.E.; Odhiambo, L.O.; Wright, W.C. Effects of vapor-pressure deficit and net-irradiance calculation methods on accuracy of standardized Penman-Monteith equation in a humid climate. *J. Irrig. Drain. Eng.* **2005**, *131*, 228–237. [CrossRef]
114. Bernacchi, C.J.; Singsaas, E.L.; Pimentel, C.; Portis, A.R., Jr.; Long, S.P. Improved temperature response functions for models of Rubisco-limited photosynthesis. *Plant Cell Environ.* **2001**, *24*, 253–259. [CrossRef]

115. Bonan, G.B.; Lawrence, P.J.; Oleson, K.W.; Levis, S.; Jung, M.; Reichstein, M.; Lawrence, D.M.; Swenson, S.C. Improving canopy processes in the Community Land Model version 4 (CLM4) using global flux fields empirically inferred from FLUXNET data. *J. Geophys. Res. Biogeosciences* **2011**, *116*, JG001593. [CrossRef]
116. Oleson, K.W.; Lawrence, D.M.; Bonan, G.B.; Drewniak, B.; Huang, M.; Koven, C.D.; Levis, S.; Li, F.; Riley, W.J.; Subin, Z.M. Technical description of version 5.0 of the Community Land Model (CLM), NCAR Tech. *Notes* **2010**, *605*, e2010NCAR-605.
117. Raj, R.; Hamm, N.; Nicholas, AS.; van der Tol, C.; Stein, A. Variance-Based Sensitivity Analysis of BIOME-BGC for Gross and Net Primary Production. *Ecol. Model.* **2014**, *292*, 26–36. [CrossRef]